2024

SINGLE-ATOM CATALYSTS FOR ELECTROCHEMICAL ENERGY CONVERSION: COPPER SINGLE-ATOM CATALYST FOR OXYGEN REDUCTION REACTION AND QUANTIFICATION OF SITE DENSITY BY CO STRIPPING VOLTAMMETRY

Dawatage Perera
University of Kentucky, shashikaperera20@gmail.com
Author ORCID Identifier:
ⓘ https://orcid.org/0000-0002-3368-8150
Digital Object Identifier: https://doi.org/10.13023/etd.2024.82

Right click to open a feedback form in a new tab to let us know how this document benefits you.

STUDENT AGREEMENT:

I represent that my thesis or dissertation and abstract are my original work. Proper attribution has been given to all outside sources. I understand that I am solely responsible for obtaining any needed copyright permissions. I have obtained needed written permission statement(s) from the owner(s) of each third-party copyrighted matter to be included in my work, allowing electronic distribution (if such use is not permitted by the fair use doctrine) which will be submitted to UKnowledge as Additional File.

I hereby grant to The University of Kentucky and its agents the irrevocable, non-exclusive, and royalty-free license to archive and make accessible my work in whole or in part in all forms of media, now or hereafter known. I agree that the document mentioned above may be made available immediately for worldwide access unless an embargo applies.

I retain all other ownership rights to the copyright of my work. I also retain the right to use in future works (such as articles or books) all or part of my work. I understand that I am free to register the copyright to my work.

REVIEW, APPROVAL AND ACCEPTANCE

The document mentioned above has been reviewed and accepted by the student's advisor, on behalf of the advisory committee, and by the Director of Graduate Studies (DGS), on behalf of the program; we verify that this is the final, approved version of the student's thesis including all changes required by the advisory committee. The undersigned agree to abide by the statements above.

<div align="right">

Dawatage Perera, Student

Doo Young Kim, Major Professor

Mark Lovell, Director of Graduate Studies

</div>

SINGLE-ATOM CATALYSTS FOR ELECTROCHEMICAL ENERGY
CONVERSION: COPPER SINGLE-ATOM CATALYST FOR OXYGEN REDUCTION
REACTION AND QUANTIFICATION OF SITE DENSITY BY CO STRIPPING
VOLTAMMETRY

_____

THESIS

_____

A thesis submitted in partial fulfillment of the
requirements for the degree of Master of Science in the
College of Arts and Science
at the University of Kentucky

By

Dawatage Shashika Madushani Perera

Lexington, Kentucky

Director: Dr. Doo Young Kim, Professor of Chemistry

Lexington, Kentucky

2024

ABSTRACT OF THESIS

SINGLE-ATOM CATALYSTS FOR ELECTROCHEMICAL ENERGY CONVERSION: COPPER SINGLE-ATOM CATALYST FOR OXYGEN REDUCTION REACTION AND QUANTIFICATION OF SITE DENSITY BY CO STRIPPING VOLTAMMETRY

Fuel cells are considered a promising technology for achieving cleaner and more sustainable energy production and utilization. However, one of the current major challenges is the economic viability associated with the extensive use of Pt group metal (PGM) catalysts, particularly on the cathode side. Therefore, non-PGM single-atom catalysts (SACs) have received considerable attention as alternatives for PGM catalysts in the oxygen reduction reaction (ORR), which occurs at the cathode of the fuel cell. Among various SAC structures, the non-PGM/nitrogen-doped carbon-based structure (M-N-C) stands out for its excellent ORR performance.

Chapter 2 illustrates the use of copper metal in place of PGM. Cu-N-C was synthesized via a simple pyrolysis method using pyrene-derived graphene quantum dots as a carbon precursor in the presence of urea as the nitrogen source. Abundant nitrogen atoms in pyrolyzed carbon network derived from graphene quantum dots enable the chelation of metal atoms, which facilitates the inclusion of a higher loading of Cu atoms. This is a significant advancement in the field of work. Cu-N-C was prepared using 24.7% copper loading, demonstrating the most promising ORR activity. Additionally, an acid-washing step was introduced to enhance the ORR catalytic activity by removing copper nanoparticles, reducing electrolyte pollution, and improving catalyst stability. This study revealed that the L2 Cu-N-C after acid washing exhibited superior performance over the before-acid-washed catalyst sample.

In Chapter 4, CO stripping voltammetry of Pt-SACs was performed to evaluate the number of active sites contributing to an electrochemical reaction. CO oxidation potential depends on particle size. This work suggests that CO stripping can be employed not only for determining the active sites based on site density (SD) but also reveals the particle size distribution.

KEYWORDS: Fuel cells, Pt group metals, Single atom catalyst, CO stripping

Dawatage Shashika Madushani Perera
Name of Student

04/01/2024
Date

SINGLE-ATOM CATALYSTS FOR ELECTROCHEMICAL ENERGY
CONVERSION: COPPER SINGLE ATOM CATALYST FOR OXYGEN
REDUCTION REACTION AND QUANTIFICATION OF SITE DENSITY BY
CO STRIPPING VOLTAMMETRY

By

Dawatage Shashika Madushani Perera

Dr. Doo Young Kim

Director of Thesis

Dr. Mark Lovell

Director of Graduate Studies

04/01/2024

Date

DEDICATION

To my parents and my husband

ACKNOWLEDGMENTS

I would like to extend my thanks to my Sri Lankan community at the University of Kentucky for always creating a joyful environment outside of my academic life. Special thanks to Janie Weatherford, my soul friend I met in Lexington; thanks for always being my home away from my home. I want to extend my heartfelt gratitude to my parents, Disna Perera and Quintas Perera, for always being my cheerleaders. Finally, I express my heartfelt gratitude to my husband, Lahiru Fernando, for his unwavering support throughout my academic journey, standing by my side every step of the way.

TABLE OF CONTENTS

LIST OF TABLES

LIST OF FIGURES

LIST OF ABBREVIATIONS

ORR	Oxygen reduction reaction
HOR	Hydrogen oxidation reaction
PEMFC	Proton exchange membrane fuel cells
RDE	Rotating disk electrode
PGM	Platinum group metals
M-N-C	Transition metal doped−nitrogen−carbon
Cu-N-C	Copper doped-nitrogen-carbon
DFT	Density functional theory
ECSA	Electrochemical active surface area
SD	Site density
Cu-SACs	Copper single-atom catalysts
Pt/WS$_2$	Pt-SAs supported on WS$_2$ nanosheets
XPS	X-ray photoelectron spectroscopy
XRD	X-ray diffraction
EDS	Energy dispersive spectroscopy
STEM	Scanning transmission electron microscopy
HAADF	High angle annular dark field
HR-TEM	High-resolution TEM
TGA	Thermogravimetric analysis

CHAPTER 1. INTRODUCTION AND LITERATURE REVIEW

1.1   Background and Motivation

In today's world, energy is vital to the operation of systems that provide basic necessities for human needs like food, shelter, work, and transportation. Developing alternative and sustainable energy sources has become trivial due to the continuous rise in global energy consumption and their impact on the environment. Among various technologies devised for this purpose, fuel cells have garnered significant attention due to their ability to operate without the use of fossil fuels and their higher efficiency in directly converting chemical energy into electric energy and power densities. Fuel cells have the potential to power a range of transportation modes, including personal vehicles, trucks, buses, marine vessels, and specialized vehicles such as lift trucks and ground support equipment. Additionally, they can serve as auxiliary power units for traditional transportation technologies. In the future, fuel cells could play a crucial role by facilitating the substitution of conventional petroleum-based fuels in cars and trucks with cleaner, lower-emission alternatives like hydrogen or natural gas.[1, 2]

Fuel cells directly transform the chemical energy present in hydrogen into electricity, producing only water and heat as byproducts. Hydrogen-powered fuel cells not only eliminate environmental pollution but also exhibit enhanced efficiency compared to traditional combustion technologies. These factors play a crucial role in addressing both the energy and environmental challenges.

A fuel cell consists of two electrodes and is surrounded by an electrolyte. The negative electrode (anode) and positive electrode(cathode). Hydrogen is sent into the anode, and the hydrogen oxidation reaction (HOR) takes place at the anode. Oxygen is fed

into the cathode, and the oxidation-reduction reaction (ORR) takes place at the cathode. At the anode, hydrogen molecules separate into electrons and protons with the help of a catalyst. The electrons go through the external circuit to the cathode and result in electricity flow. In an acidic electrolyte medium, the protons move through the electrolyte towards the cathode. They react with oxygen and electrons and result in water and heat with the support of a catalyst at the cathode.

Consequently, efficient catalysts for the ORR are essential for converting electrochemical energy in fuel cells. The slow kinetics of the ORR at the cathode limit the performance of the fuel cells. This is due to the stability of the oxygen double bond (498 kJ/mol) and the sluggishness of the activation process.[3]

At present Pt or Pt alloys are considered as the state of art catalysts for ORR. However, limited availability, higher cost, low durability, and poor tolerance to methanol and carbon monoxide (CO) of Pt group metal (PGM) catalysts significantly affect their widespread use in large-scale applications. As a result, efforts have been made to create ORR catalysts to replace Pt. Non-platinum group metal (non-PGM) based ORR electrocatalysts emerged as promising alternatives to Pt due to their abundance, cost-effectiveness, performance, and stability.[4, 5]

1.2   Electrocatalysis

In 1835, Jons Jakob Berzelius, a Swedish chemist, introduced the term "catalysis." In the 19th century, German Scientist Wilhelm Ostwald proposed a universally accepted definition: "A catalyst is a substance which increases the rate of a chemical reaction without being consumed in the process."[6]
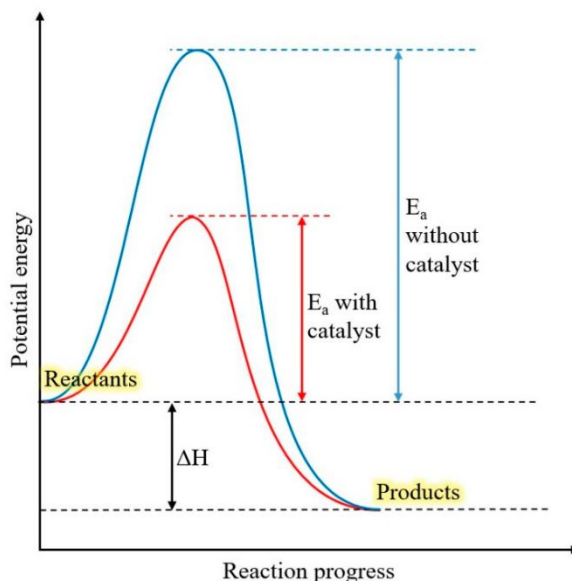
Figure 3.1: The impact of a catalyst on the potential energy profile.[7] Reprinted with permission from Sinar Mashuri, S.I., Ibrahim, M.L., Kasim, M.F., Mastuli, M.S., Rashid, U., Abdullah, A.H., Islam, A., Asikin Mijan, N., Tan, Y.H., Mansir, N., Mohd Kaus, N.H., Yun Hin, T.-Y., 2020. Photocatalysis for Organic Wastewater Treatment: From the Basis to Current challenges for society. Catalysts 10, 1260. https://doi.org/10.3390/catal10111260

Figure 1.1 shows the effect of a catalyst in a hypothetical exothermic reaction. In the presence of the catalyst, the reaction occurs through an alternative pathway that requires less energy.[7] The use of catalysts can be expanded to include electrocatalysis. An electrocatalyst is a specialized type of catalyst involved in electrochemical reactions. Most of the time, it functions as the electrode surface. The electrocatalyst transfers electrons between the reactant and electrode. It modifies the electrochemical reaction pathway, increases the rate of reaction, and decreases the activation energy barrier. The ideal electrocatalyst is not consumed during the reaction process.[8] Additionally, the outcome and the overall thermodynamics remain unchanged.[9]

3

1.2.1 Electrochemical reactions

Electrochemical reactions usually consist of two half-reactions, namely cathodic and anodic reactions. Those reactions occur within an electrochemical cell, which is also a redox system. An electrochemical cell consists of a cathode, anode, electrolyte, semi-permeable membrane, and an external circuit that facilitates the transfer of electrons. The potential energy gradient between the electrode-electrolyte interface controls the rate of electron transfer across electrodes and redox species.[1] In order to obtain a comprehensive understanding of a complex electrode reaction process, it is necessary to understand the kinetic and thermodynamic aspects of each individual step involved.[10]
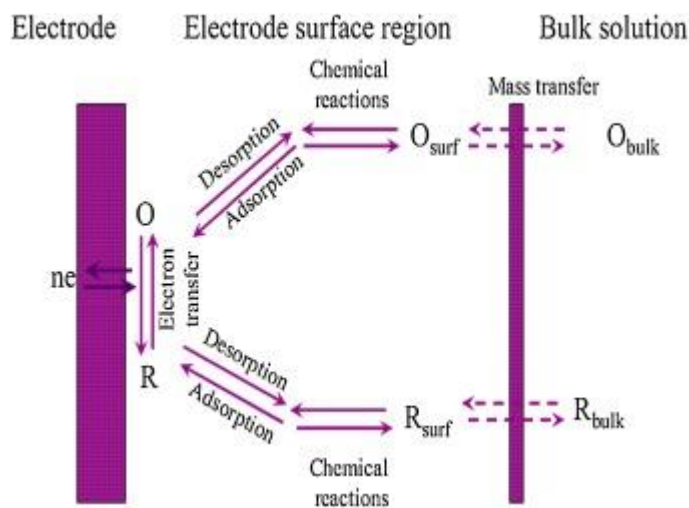
Figure 1.4: The general electrode reaction pathway.[11]Reprinted from Process Biochemistry, Volume 91, Elahe Abedi, Mohammad Javad Amiri, Mohammad Ali Sahari, Kinetic, isotherm, and thermodynamic investigations on adsorption of trace elements and pigments from soybean oil using high voltage electric field-assisted bleaching: A comparative study, Pages 208-222, Copyright (2019), with permission from Elsevier.

As shown in Figure 1.2, in addition to mass transfer and electron transfer, various fundamental processes can occur during electrode reactions. The steps involved in this process are as follows: the reactants are adsorbed through a covalent bond or electrostatic interactions, next chemical reactions occur through the formation of chemical bonds or cleavage, and then phase formation takes place, such as the formation of the oxide layer in metals and finally, multiple electron transfers occur and are separated by chemical reactions.[12]

1.2.2 Thermodynamic aspects of electrode reaction

The thermodynamic approach of electrochemical reaction focuses on the Gibbs free energy difference (ΔG). This is related to the direction of the overall reaction. If the change in Gibbs free energy is less than zero, it indicates that the forward reaction is thermodynamically favored and will occur spontaneously. If the change in Gibbs free energy is higher than zero, it indicates that the forward reaction is non-spontaneous, meaning that energy needs to be supplied in order to drive the reaction. And if the $\Delta G = 0$, it implies that the reaction is in equilibrium.[13]

1.2.3 Kinetics of the electrode reaction

The kinetic properties of electrode reactions define the correlation between faradaic current and overpotential (η). The term "overpotential" refers to the electrode potential required to generate a specific current in an electrochemical reaction. It is calculated as the difference between the applied potential and the equilibrium potential. Overpotential can be categorized into three distinct types: activation overpotential(η_a), concentration overpotential(η_c), and Ohmic loss(η_o). The activation overpotential(η_a), refers to the

potential needed to overcome the activation energy of the cell reaction in order to produce a specific current.[2] The concentration overpotential(η_c) is caused as a result of mass transport limitation.[14] Ohmic loss(η_o) is the voltage drop brought on by ions moving through the electrolyte and membrane and electrons transferring throughout the electrical circuit.[15]Hence, a primary objective of electrocatalysis research is to identify electrode materials that can minimize the activation overpotential ηa.

The Butler-Volmer equation is the fundamental equation for electrode kinetics. It describes the correlation between the exchange current density(i_0) and the electrode activation overpotential (η_a).

$$i = i_o \left\{ e^{\left[\frac{-(\alpha)F\eta_a}{RT} \right]} - e^{\left[\frac{(1-\alpha)F\eta_a}{RT} \right]} \right\}$$

The net current, denoted as "i", is determined by the first and second exponential terms, which represent the cathodic and anodic terms, respectively. The transfer coefficient denotes as "α". The key assumption in formulating the equation is that the electrolyte solution at the electrode is thoroughly stirred, and the current is maintained at such a low level that the concentrations at the electrode surface do not significantly deviate from the bulk solution.

Overpotentials above approximately 50 mV are applicable to the linear dependence between η_a and $\log|i_c|$, which we call the Tafel equation. As a result, when the current density is near zero, the equation cannot be applied. The following linear relationship was obtained when the reduction reaction was dominant.[16]

$$i_c = i_o e^{\left[\frac{-(\alpha)F\eta_a}{RT} \right]}$$

$$log|i_c| = log(i_o) - \left[\frac{(\alpha)F}{RT}\right]\eta_a$$

1.2.4 Sabatier principle for electrocatalysis

According to the Sabatier principle, in an ideal catalyst, the interaction between the catalytic active site and adsorbate should neither be too strong nor too weak. This allows for a qualitative explanation of the electrocatalytic activity. An interaction that is excessively strong prevents the products from desorbing, whereas a weak interaction causes insufficient reactant activation.[17] The relationship between catalytic activity and bond strength of the reaction intermediates can be illustrated by the volcano plot, as shown in Figure 1.3.
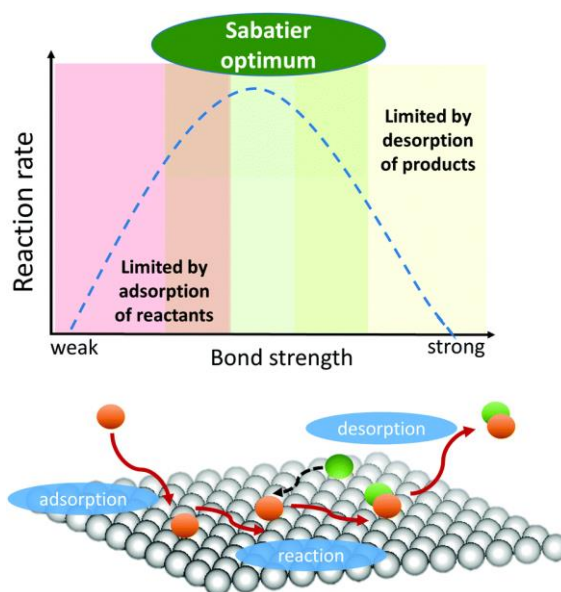
Figure 1.5: The top image depicts a schematic representation of a Sabatier volcano-type plot, illustrating the relationship between the catalytic reaction rate and the bond strength of the reaction intermediate. The image at the bottom displays the interaction between two molecules, represented by green and orange balls, along with the sequential stages of the reaction.[17] Reprinted from Chemical Communications, Volume 56, Sebastián-Pascual,

Paula; Jordao Pereira, Inês; Escudero-Escribano, Maria, Tailored electrocatalysts by controlled electrochemical deposition and surface nano-structuring, Pages 13261-13272, Copyright (2020), with permission from Royal Society of Chemistry.

1.2.5 Effects of mass transfer

The faradaic current at any given moment directly reflects the rate of the electrochemical reaction happening at the electrode. The magnitude of this electrical current is determined by two primary factors: mass transport, which governs the speed at which material reaches the electrode from the surrounding solution, and charge transfer kinetics, which controls the rate of electron transfer across the interface. These processes are important in regulating the flow of electric current. Mass transport includes three fundamental mechanisms: diffusion, migration, and convection (Figure 1.4).[18]
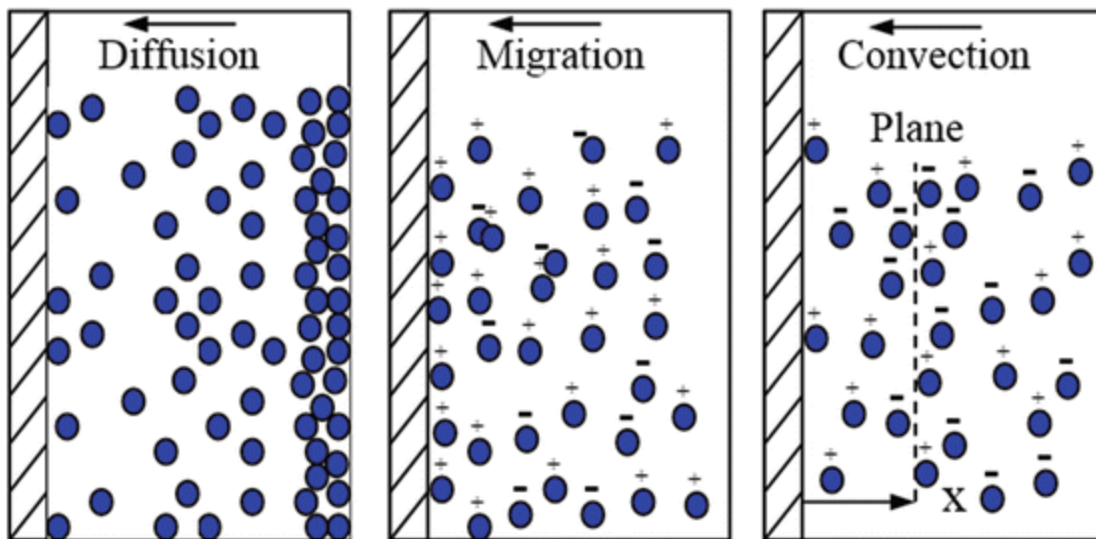
Figure 1.6: Modes of mass transfer.[18] Reprinted from Perez, N., Mass Transport by Diffusion and Migration. In Electrochemistry and Corrosion Science, Perez, N., Ed. Springer International Publishing: Cham, 2016; pp 151-197. Copyright (2016), with permission from Springer.

Diffusion refers to the spontaneous movement of molecules from a region with a higher concentration to a region with a lower concentration. Migration is the term used to describe the movement of charged particles in response to a local electric field. Hydrodynamics is the study of fluid motion. In electrochemistry, forced movement of solution species through mechanical (stirring) or other means is referred to as convection. In experimental setups, a rotating disk electrode (RDE) is commonly employed to enhance the electrolyte flow through convection.

1.3 Introduction to Oxygen Reduction Reaction

The oxygen reduction reaction (ORR) plays a vital role in numerous biological processes, including respiration, as well as in energy conversion systems such as metal-air batteries and fuel cells. ORR primarily takes place in aqueous solutions through two pathways: the direct transfer of four electrons from O_2 to H_2O, and the transfer of two electrons to hydrogen peroxide (H_2O_2).[19] Superoxide (O^{2-}) can also be formed through a one-electron transfer pathway in nonaqueous aprotic solvents or alkaline solutions.[20] In proton exchange membrane (PEM) fuel cells, which comprise hydrogen/oxygen and methanol/oxygen (direct methanol) fuel cells, the oxygen reduction reaction (ORR) occurs at the cathode. Nevertheless, the kinetics of oxygen reduction reaction (ORR) are generally slow. Therefore, it requires efficient catalysts to enhance the reaction rate in the fuel cell operation. Currently, platinum (Pt) catalysts are widely used. However, their extensive commercial application is limited due to their high cost and rareness. Therefore, over the past few decades, a lot of research has been conducted in designing non-noble metal catalysts as alternatives.[4]

1.3.1 Thermodynamics and Electrode Potential of ORR

Table 1.1 displays the chosen ORR processes and their respective thermodynamic electrode potentials under standard conditions. All potentials were given relative to the standard hydrogen potential (V vs SHE). SHE is defined as zero under a 1.0 M proton aqueous solution at 1.0 atm hydrogen gas pressure and at any temperature. The thermodynamic electrode potentials were given in both an acidic aqueous solution and an alkaline aqueous solution. The electrode potentials provided in Table 1.1 are at 25^0C, 1.0 atm.

Table 1.1. Electrode potentials of the ORR in acidic and alkaline aqueous medium at 25°C and 1.0 atm.

Oxygen reduction Reactions	E^0 (V vs SHE)	Condition of the Electrolyte
$O_2 + 4H^+ + 4e^- \rightleftarrows 2H_2O$	1.229	Acidic aqueous solution
$O_2 + 2H^+ + 2e^- \rightleftarrows H_2O_2$	0.70	Acidic aqueous solution
$H_2O_2 + 2H^+ + 2e^- \rightleftarrows 2H_2O$	1.76	Acidic aqueous solution
$O_2 + H_2O + 4e^- \rightleftarrows 4OH^-$	0.401	Alkaline aqueous solution
$O_2 + H_2O + 2e^- \rightleftarrows HO_2^- + OH^-$	-0.065	Alkaline aqueous solution
$HO_2^- + H_2O + 2e^- \rightleftarrows 3OH^-$	0.867	Alkaline aqueous solution

The reactions listed in Table 1.1 are known as half-cell reactions. Practically, these reactions cannot happen unless there are half-cell reactions that provide electrons. Within an electrochemical cell, two distinct half-cell reactions occur: the anode reaction and the cathode reaction. For instance, in an H_2/O_2 fuel cell, there are two half-cell reactions:

$At\ Anode: H_2 \rightleftarrows 2H^+ + 2e^-, E^0 = 0.00\ V\ vs\ SHE$
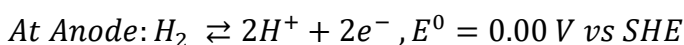
$$At\ Cathode: \frac{1}{2}O_2 + 2H^+ + 2e^- \rightleftarrows H_2O, E^0 = 1.229\ V\ vs\ SHE$$

According to the above reactions, the anode electrode potential is 0.00 V vs SHE, the cathode electrode potential is 1.229 V vs SHE. By using these two half-cell reactions, the construction of a fuel cell would result in the overall cell reaction given below.

$$\frac{1}{2}O_2 + H_2 \rightleftarrows H_2O, E^0_{cell} = 1.229\ V\ vs\ SHE$$

As stated above, the overall fuel cell has a thermodynamic cell voltage of 1.229 V (vs SHE) under reversible conditions. Therefore, the standard free energy change of the overall fuel cell reaction is given by, $\Delta G^0_{cell} = -nFE^0_{cell}$, n represents the number of electrons transferred in the overall reaction (in this case n = 2), and F represents Faraday constant, (96,745 C/mol). If ΔG is negative, it indicates that the corresponding cell reaction should occur spontaneously under standard conditions.[13]

1.3.2 Oxygen Reduction Reaction (ORR) on Pt-based Catalysts

Pt-based electrocatalysts are preferred for commercial applications in order to enhance the rate of ORR due to their exceptional activity (low overpotential and high current density and stability, as compared to non-noble metal catalysts. In the last twenty years, significant efforts have been made to comprehend the theoretical aspects that influence the ORR performance of electrocatalysts based on Pt, as well as to create novel synthesis methods that can improve the rate of ORR.

As previously discussed, ORR can yield either H_2O_2 or H_2O as final products. The specific outcome depends on whether the process follows the two-electron pathway or the four-

electron pathway. In Proton Exchange Membrane Fuel Cells (PEMFCs), it is preferable to have a four-electron pathway that minimizes the release of peroxide. This is because H_2O_2 has been found to cause damage to the Nafion membrane by breaking down into extremely reactive intermediates, which ultimately leads to a decline in the performance of the fuel cell.[21]

The initial step in oxygen reduction reaction involves the adsorption of oxygen onto the Pt atoms. In conventional Pt nanoparticle catalysts, only the surface Pt atoms serve as active sites. Therefore, in order to enhance the quantity of active Pt sites per unit mass, it is essential to optimize the exposure of Pt atoms on the surface. In simpler terms, this means increasing the ratio of Pt atoms on the surface compared to those in the interior throughout the entire volume. Typically, this involves two factors: increasing the loading of Pt and preventing the obstruction of surface Pt atoms in the surface of the catalyst structure. The size of Pt particles has a major impact on the number of active sites per unit mass. Decreasing the size of Pt particles and transforming them into nano crystals from their bulk form are two effective strategies to improve the activity of the ORR.[22]

1.3.3   Heteroatom-doped carbon material

Graphene, a 2D carbon sheet arranged in a honeycomb lattice structure, has gained significant attention since its discovery in 2004. Its remarkable electrical conductivity, specific surface area, electrochemical stability, and tunable band gap make Graphene a promising material for a wide range of applications, including rechargeable transistors, lithium-ion batteries, highly sensitive sensors, supercapacitors, and fuel cells.[23]

In recent years, there has been significant interest in incorporating heteroatoms, such as nitrogen(N), boron(B), sulfur(S), and phosphorus(P) into the basal plane of carbon structure.[24] N doping on carbon nanostructures is commonly reported due to its similar atomic size to carbon and the presence of five valence electrons, which facilitates its incorporation into the basal plane of the carbon structure. It is reported in the literature that when nitrogen is added to the carbon plane, it changes the shape and electron-donating properties of the nanocomposite. This is achieved by redistributing the electronic density of the nearby carbon atoms, which creates an electrophilic center near the N atoms.[25]
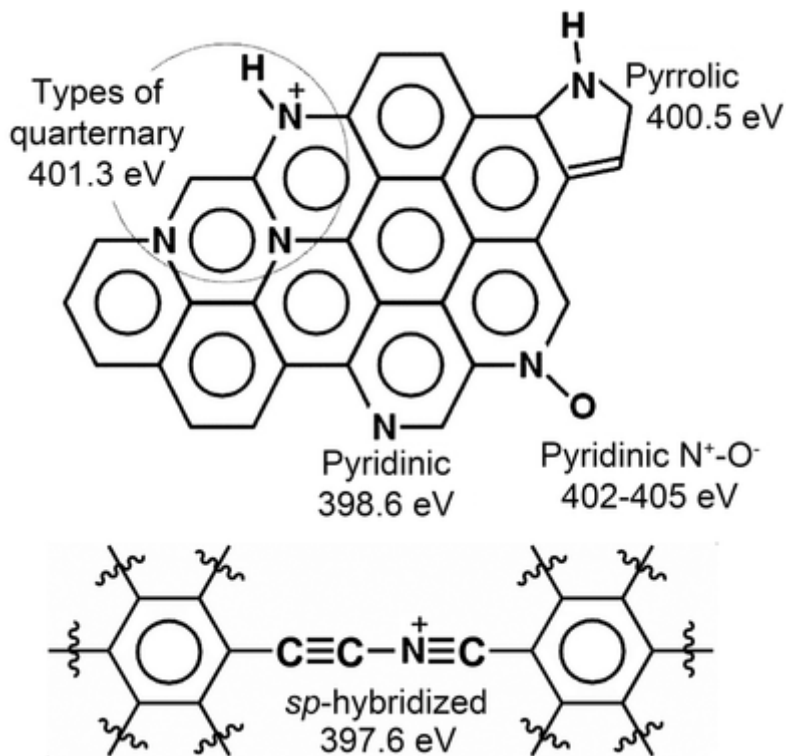
Figure 1.5:The nitrogen species commonly found in N-doped carbon materials and their corresponding binding energies in X-ray photoelectron spectroscopy (XPS) are indicated.[26] Reprinted from Yang, L.; Shui, J.; Du, L.; Shao, Y.; Liu, J.; Dai, L.; Hu, Z. Carbon-Based Metal-Free ORR Electrocatalysts for Fuel Cells: Past, Present, and Future. Advanced

As shown in figure 1.5, there are four main forms of nitrogen species in C nanomaterials that have been reported in the literature: pyrrolic, pyridinic, pyridinic-N-oxide, and graphitic (quaternary N). Pyridinic-N and graphitic-N are sp^2 hybridized, while pyrrolic-N is sp^3 hybridized. Figure 1.6 demonstrates the electron configurations for the main forms of nitrogen function groups mentioned above. The pyridinic-N forms bonds with two carbon atoms located at the defects or edges of graphene and donates one p electron to the π system. Pyrrolic-N refers to nitrogen atoms that donate two p electrons to the π system. Quaternary-N (Graphitic-N) refers to nitrogen atoms that replace C atoms in the hexagonal ring structure.[25]
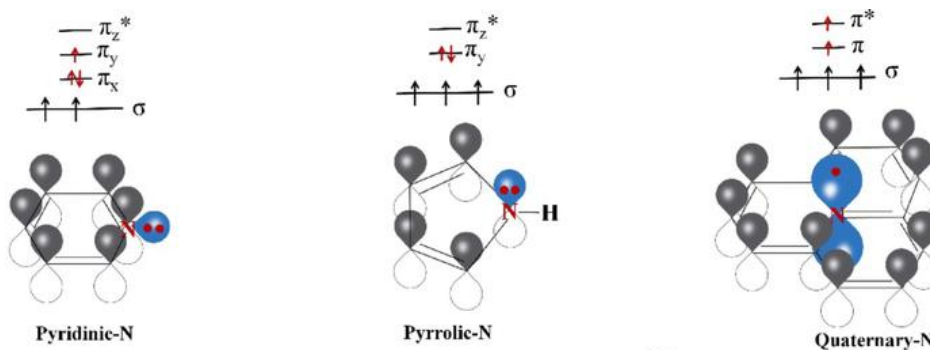
Figure 1.7: Electron configuration of Pyridinic-N, pyrrolic-N, and quaternary-N. Adapted with permission.[27] Reprinted from Li, R.; Huang, J.; Li, J.; Cao, L.; Luo, Y.; He, Y.; Lu, G.; Yu, A.; Chen, S. Nitrogen-Doped Hard Carbon on Nickel Foam as Free-Standing Anodes for High-Performance Sodium-Ion Batteries. *ChemElectroChem.* **2020**, *7* (3), 604-613. DOI: 10.1002/celc.201901770. Copyright 2019, Wiley-VCH.

Research has been conducted to replace expensive platinum-based catalysts with affordable transition metals such as Cu, Fe, Co, and Ni for catalyzing sluggish oxygen reduction reactions. The interaction between a transition metal and an unsaturated nitrogen species occurs through the formation of a σ bond. This bond is formed when a filled π bonding molecular orbital from the unsaturated nitrogen species donates electrons to an empty d orbital of the metal. Subsequently, there is a π back-donation from the filled d π orbital of the metal to the empty π* antibonding molecular orbital of the unsaturated nitrogen species. This interaction exhibits charge transfer, which is a common feature of a covalent chemical bond with a divalent transition metal that has partial ionic characteristics. However, the graphitic-N sites form a covalent bond with transition metals.[25, 28]

Among the N functional groups discussed earlier, pyridinic-N is thought to be linked to ORR activity. This is because it has a lone pair of electrons, which is considered an active catalytic center, as reported in previous studies.[5] In addition, certain studies propose that pyrrolic nitrogen species are accountable for the performance of ORR in the alkaline medium.[29]

1.3.4   Cu-N-C single atom catalyst for ORR

Recent studies suggest that transition metal doped−nitrogen−carbon (M-N-C) catalysts, which are cost-effective and efficient, are promising alternatives to expensive Pt catalysts in applications like fuel cells, particularly for the ORR. Potentially suitable catalysts for the ORR can be discovered in natural biological systems. For example, laccase, which possesses Cu−N coordination structures as the active site, can catalyze the ORR.[30]

The catalytic performances of Cu-N-C materials are primarily influenced by the quantity and arrangement of the active sites. They are strongly dependent on material synthesis conditions such as pyrolysis temperature, duration, atmosphere, and the bonding between various precursors. In the literature, $Cu-N_2$, $Cu-N_3$, and $Cu-N_4$ have been proposed as the active sites for ORR in Cu-N-C catalysts.[31]
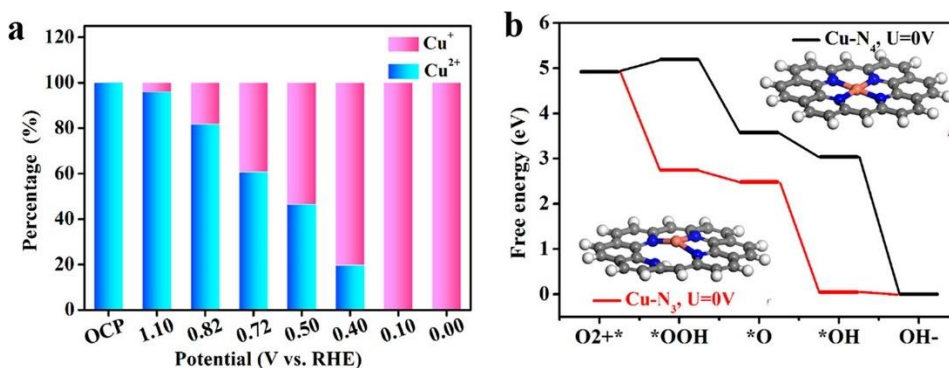
Figure 1.8:(a) The distribution of Cu^{2+} and Cu^+ ions at various applied potentials. (b) Free energy plot illustrating the ORR on $Cu-N_3$ and $Cu-N_4$ sites.[31] Reprinted with permission from Yang, J.; Liu, W.; Xu, M.; Liu, X.; Qi, H.; Zhang, L.; Yang, X.; Niu, S.; Zhou, D.; Liu, Y.; et al. Dynamic Behavior of Single-Atom Catalysts in Electrocatalysis: Identification of $Cu-N_3$ as an Active Site for the Oxygen Reduction Reaction. Journal of the American Chemical Society 2021, 143 (36), 14530-14539. Copyright 2021, American Chemical Society.

The dynamic evolution of the active site is a common occurrence in catalysis. In the electrochemical reactions facilitated by M-N-C materials, the dynamic evolution of the M-N_x moiety can be influenced by both the applied potential and adsorption of reactants/intermediates. Recent studies have demonstrated that operando X-ray absorption near edge structure (XANES) spectroscopy can clearly detect the potential-driven dynamic

transformation from Cu^{2+}-N_4 to Cu^+-N_3 and subsequently to HO-Cu^+-N_2 during the operation of the ORR.[32] The increase in the Cu^+/Cu^{2+} ratio due to the applied potential indicates that the Cu^+-N_3 moiety with low coordination is the actual active site.[31] As shown in Figure 1.7, this is further confirmed by the significantly lower free energy of each individual step of the ORR on Cu^+-N_3 compared to Cu^{2+}-N_4, as determined by density functional theory (DFT) calculations.[31]

1.4   CO stripping technique

The CO stripping method allows the precise determination of the electrochemical active surface area (ECSA) of Pt-group metal-based catalysts in both acidic and alkaline media. This method ensures precise measurements of ECSA by verifying the thorough CO adsorption and CO oxidation. In addition, the potential window for CO stripping has very little or no overlap with most other electrochemical reactions.

From a mechanistic perspective, CO electrochemical oxidation is thought to take place through the adsorption of CO and oxygen-containing molecules, typically identified as OH. The simplified reaction mechanism is shown by the following reactions.

$$H_2O + Pt \rightleftarrows Pt - OH_{ad} + H^+ + e^- \hspace{4cm} \text{Step 01}$$

$$Pt - CO_{ad} + Pt - OH_{ad} \rightleftarrows CO_2 + H^+ + e^- + 2Pt \hspace{2cm} \text{Step 02}$$
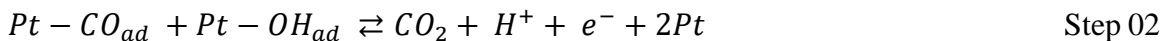
During step 1, oxygen-containing species, referred to as OH_{ad}, are generated by oxidizing water on unoccupied Pt sites. The conversion of CO to CO2 is achieved through step 2: adsorbed CO molecules react with adsorbed OH_{ad} molecules, resulting in the production of CO_2, H+, an electron, and two available Pt sites. The overall process requires 2 Faradays

per mole of reaction. Reaction (2) is considered a Langmuir-Hinshelwood type of reaction as it involves the interaction of two adsorbed molecules on the surface. Hence, the movement of the adsorbed species on the surface and the locations where the reaction takes place is crucial for understanding the entire process.[33, 34]

While Reactions (1) and (2) offer a comprehensive explanation of the CO oxidation process, other researchers have put forth a more complex mechanism that includes the presence of an adsorbed intermediate like adsorbed $COOH_{ad}$.[35] The following three scenarios can be used to conduct fundamental electrochemical studies on the oxidation of CO: i) CO stripping, as we discussed before, ii) CO-contaminated H_2 gas iii) CO oxidation continuously as a bulk.[36] In this study, CO stripping is considered since our primary goal is to determine the electrochemical surface area/ active sites based on the peak area resulting from CO stripping.

1.5   Thesis Organization

In recent years, transition metal-based single-atom catalysts (SACs) have received significant attention and have proven to be promising catalysts for ORR. Nevertheless, their overall performance in terms of overpotential, selectivity, and current density needs further improvements. Therefore, a fundamental understanding of catalyst sites and reaction mechanisms should be investigated to develop better catalysis.

Chapter 2 of this thesis investigates the significance of an acid-washing step on the ORR of copper single-atom catalysts (Cu-SACs). Additionally, X-ray photoelectron spectroscopy (XPS) was utilized to study the chemical properties of the Cu-SACs, while thermogravimetric analysis (TGA) offered insights into the copper loading. Furthermore,

the crystallinity of the copper catalysts was analyzed via X-ray Diffraction (XRD), and their morphology was determined using HR-STEM. Finally, the electrochemical ORR performance was evaluated under half-cell conditions.

As part of a collaborative work, chapter 3 of this thesis proposes the CO stripping method to determine the electrochemical active sites of Pt single atoms supported on tungsten disulfide (WS_2) nanosheets (Pt/WS_2 catalyst). The XRD and high-resolution scanning transmission electron microscopy (HR-STEM) were employed to analyze the crystallinity and morphology of the material. The determination of the CO stripping voltametric charge was obtained through electrochemical measurements.

Chapter 4 will focus on the conclusions drawn from the studies conducted and outline future aspects for further exploration.

CHAPTER 2. COPPER-INCORPORATED GRAPHENE-QUANTUM-DOT DERIVED
SINGLE-ATOM CATALYST FOR OXYGEN REDUCTION REACTION.

2.1   Introduction

In order to make proton exchange membrane fuel cells (PEMFCs) commercially viable, it

is crucial to substantially reduce the costs associated with their production. Currently,

platinum group metal (PGM) catalysts are crucial components in the manufactured

membrane electrode assemblies, constituting approximately 25% of the total fuel cell

expenses. Consequently, there is a critical demand to develop PGM-free catalysts for the

practical implementation of PEMFCs.[37]

In recent years, there has been an enormous growth of interest in single-atom catalysts

(SACs). By reducing metal particle size to the single-atom level, thereby achieving

homogeneously distributed active sites, SACs typically exhibit significantly enhanced

catalytic activity. The size reduction of metal nanoparticles can alter their catalytic

behavior through various mechanisms, including quantum size effects, surface effects,

cluster configurations, and metal-support interactions. It is worth noting that the local

coordination environments can profoundly influence their physicochemical properties.

Increasing the density of active sites and the corresponding intrinsic activity are generally

pivotal strategies for improving the performance of many catalyst systems. SACs,

characterized by isolated metal atoms dispersed or anchored on different supports,

currently represent one of the most crucial catalyst systems due to their maximum atom

efficiency, presence of well-defined reaction mechanisms, and unsaturated active sites.[38]

Among various catalyst structures, the transition metal/nitrogen-doped carbon-based structure (M-N-C) stands out for its excellent oxygen reduction reaction (ORR) performance. The substrate on which the metal single-atom catalysts (SACs) are dispersed has been shown to be crucial.[39] Graphene, with its sp^2-hybridized carbon structure, serves as an ideal substrate for dispersing metal SACs due to its exceptional electrical conductivity, large specific surface area, remarkable mechanical strength, and high flexibility.[40] Additionally, the presence of pyridinic N acts as a 'coordinator,' effectively protecting and stabilizing the single atomic metals in the catalysts. However, due to the limited amount of nitrogen species in the precursor, the content of catalytically active single atomic metals in the catalysts has remained relatively low(<1 wt.%).[41]

The loading of metal SACs onto graphene and other substrates is usually low because metal atoms tend to aggregate. This aggregation presents a significant barrier to the practical application of metal SACs. The conventional method for fabricating graphene-based SACs involves the high-temperature pyrolysis of graphene oxide along with metal salts. However, single-atom metals are thermodynamically unstable and tend to agglomerate into clusters or even nanoparticles during the pyrolysis process due to their higher surface energy. Additionally, higher metal loadings often lead to the formation of inorganic iron species. To resolve this problem, only a limited quantity of metal salt can be added to the precursors.[42] The loading level of single-atom metals on graphene is currently unsatisfactory, and achieving high loading of isolated single atoms remains challenging. Furthermore, this limitation is a critical barrier against the technical development of SACs because of the low concentrations of active sites.

In response, significant efforts have been directed towards developing non-noble metal-based catalysts with higher metal loading, aiming for efficient and cost-effective solutions for electrochemical oxygen reduction. Here, we have prepared a synthesis method that effectively eliminates inorganic metal by-products and unbound free-standing metal nanoparticles from the Cu-N-C catalyst through a straightforward pyrolysis process followed by acid-leaching. This purification treatment results in the removal of nearly all inorganic by-products and Cu nanoparticles, leaving behind only Cu-N-C sites. More importantly, the treatment results in enhanced ORR activity rather than a decrease, highlighting its effectiveness.

The work employed high-resolution scanning transmission electron microscopy (HR-STEM) to precisely determine the microstructure of Cu-SACs. X-ray photoelectron spectroscopy (XPS) was used to investigate the chemical properties of the Cu-SACs, while thermogravimetric analysis (TGA) and XPS provided insight into the Cu loading. Furthermore, the absence of nanoparticles is also confirmed through X-ray Diffraction (XRD), XPS, and HR-STEM studies showing the effective formation of Cu-SACs on the graphitic matrix.

2.2   Experimental

2.2.1   Preparation of Cu-SAC

2.2.1.1 GQDs–NH2 synthesis

Pyrene (2 g, purity of 98%, ACS grade) underwent nitration to produce tri-nitropyrene in hot nitric HNO_3 (160 ml, purity of 68-70%, ACS grade) at 80 °C under reflux and stirring for 12 hrs. Following cooling to room temperature, the resulting mixture was diluted with deionized (DI) water (1 l) and then filtered through a microporous membrane (0.22 mm) to eliminate the acid. The resulting yellow 1,3,6-trinitropyrene (1.0 g, yield of 90%) was dispersed in a KOH solution in DI water (200 ml, 0.2 M) through ultrasonication in an ice bath (500 W, 40 kHz) for 2 hrs. The suspension was then transferred to a poly(tetrafluoroethylene) (Teflon)-lined autoclave (500 ml) and heated at 200 °C for 10 hr. Upon reaching room temperature, the product, which included water-soluble graphene quantum dots (GQDs), underwent filtration using a microporous membrane (0.22 mm) to remove any insoluble carbon by-products. Subsequently, it went through a two-day dialysis process in a dialysis bag with a retained molecular weight of 1000 Da to remove sodium salt and any remaining unfused small molecules.

2.2.1.2 Cu–N–C (Cu-SAC) synthesis

Initially, $CuSO_4$ (1 g, purity 99.5 %, ITB) was dissolved into DI water (200 ml) to prepare the $CuSO_4$ stock solution (5 mg/ml). Then, x ml of $CuSO_4$ stock solution (to obtain 15 %, 40 % & 60 % nominal Cu loading) was added to 30 ml of purified GQDs–NH2 solution (1 mg/ml), followed by sonication in ice bath for 30 min. The above solution was freeze dried and mixed with urea (VWR) with a mass ratio of 1:10, and further heated in a tube furnace to 500 °C under a gas flow of 100 sccm Ar (UHP, Airgas) over 2 hrs, and maintained the same temperature for an additional 1 hr before being cooled to room temperature. Following this, the pyrolyzed sample underwent acid leaching in a continuous stirring in HCl solution (2 mol L^{-1}) for 2 hrs. The resulting suspensions were then filtrated, washed

with DI water, and dried at 40 °C. Finally, the Cu-SAC was collected for further characterization.

The nominal Cu loading was defined using the following equation:

$$Nominal\ Cu\ Loading = \frac{Mass\ added_{Cu(mg)}}{Mass\ added_{Cu(mg)} + Mass_{GQDs\ (mg)}} \times 100$$

2.2.2 Material Characterization

Thermogravimetric analysis (TGA) was performed to determine the metal weight percentage in Cu-SACs. The analysis was conducted in an air, temperature ranging from 30°C to 750°C at a rate of 20°C/min using the TA Instruments TGA 5500. The crystalline structure and phases of all samples were assessed utilizing the BRUKER AXS D8 ADVANCE X-ray diffractometer, which was equipped with CuKα radiation (1.54 Å) and a LYNXEYE (1D mode) detector, with an incremental measurement step of 0.01°.

For elemental composition and chemical state analysis, X-ray photoelectron spectroscopy (XPS) was employed, utilizing a Thermo Scientific K-alpha X-ray photoelectron spectrometer with monochromatic Al Kα radiation (energy of 1486.6 eV). The spot diameter analyzed by XPS was 400 μm, and an electron flood gun was utilized to mitigate surface charging. High-angle annular dark-field (STEM-HAADF) imaging with aberration correction was carried out using the Nion UltraSTEM 100 at 100 kV to examine the samples structure in detail. Furthermore, the JEOL NEOARM aberration-corrected analytical TEM/STEM system was employed to gather data through energy dispersive X-ray spectroscopy (EDS).

2.2.3 Electrochemical Characterization

2.2.3.1 Preparation of a rotating disk electrode (RDE)s

For electrochemical measurements, the preparation of a Rotating Disk electrode (RDE) involved the following steps: The glassy carbon disk electrode (geometric area: 0.07 cm^2), underwent polishing using alumina powder (0.05 micron). Afterward, Cu-SAC catalyst (1 mg), carbon black (1 mg), and Nafion (20 μL, fuel cell store, 5 wt% in ethanol) were mixed in 1 ml of deionized water. Then it was subjected to one hour of sonication to achieve a homogeneous catalyst ink with a concentration of 1 mg/ml. Subsequently, 30 μL of this ink was mounted on the glassy carbon electrode through drop-casting. The electrode was then dried overnight in an oven at 60 °C.

2.2.3.2 Electrochemical Performance Test

The electrochemical experiments were conducted using a CHI 760D potentiostat (CH Instruments, USA) within a single-compartment electrochemical cell. These measurements followed a conventional three-electrode cell setup, where Ag/AgCl (CH Instruments), Pt wire, and RDE were designated as the reference (RE), counter (CE), and working electrodes (WE), respectively.

The analysis of the catalytic performance of each Cu-SAC towards the ORR was carried out in a KOH solution (0.1 molL^{-1}) saturated with O$_2$. Cyclic voltammetry (CV) curves for the catalysts were recorded in a N$_2$ saturated KOH solution (0.1 molL^{-1}) at a scan rate of 50 mV s^{-1}. For the ORR assessment, linear sweep voltammetry (LSV) was performed in an O$_2$ saturated KOH solution (0.1 molL^{-1}) at a scan rate of 10 mV s^{-1}, while varying the electrode rotation rate from 600 rpm to 1600 rpm. The catalytic activities of Cu-SACs with

different weight percentages (L1, L2, and L3) were compared to that of commercial 20 wt.% Pt/C as a reference.

The electron transfer number (n) for the catalyst concerning the ORR was determined using the Koutecky-Levich equation provided below:

$$\frac{1}{j} = \frac{1}{j_D} + \frac{1}{j_K} = \frac{1}{B\omega^{\frac{1}{2}}} + \frac{1}{j_K}$$

$$B = 0.2nF(D_{O_2})^{2/3}v^{-1/6}C_{O_2}$$

Where j represents the current density (A/cm^2) measured on RDE, j_D and j_K denote the diffusion and kinetic current densities respectively. B corresponds to the slope of Koutecky-Levich (K-L) plot, and ω represents the electrode rotating rate (rpm). The F stands for the Faraday constant (96495 Cmol^{-1}), D_{O_2} is the diffusion coefficient of oxygen in 0.1 molL^{-1} KOH(1.9 x 10^{-5}cm^{2}s^{-1}), v is the kinetic viscosity of the electrolyte (0.01 cm^{2}s^{-1}) and C_{O_2} is the saturated concentration of oxygen molecules in water (1.2 x 10^{-6} mol cm^{-3}) at room temperature, n denotes the quantity of electrons transferred per oxygen molecule. The value of 0.2 is utilized as a constant when the rotation speed is stated in rpm.

Moreover, the catalytic durability was assessed in a KOH solution (0.1 molL^{-1}) saturated with O$_2$ at a rotation rate of 1600 rpm, employing a scan rate of 50 mV s^{-1}, from 0.3 V to -1 V for 250 cycles. To comprehensively comprehend alterations in catalytic activity, couple of LSVs were conducted before and after the 250 cycles, at a rotation rate of 1600 rpm and a scan rate of 10 mV s^{-1}.[43]

2.3 Results & Discussion

2.3.1 Characterization of Cu-N-C

Three Cu-N-C samples were synthesized following the synthesis protocol, each containing varying percentages of Cu labeled as L1 Cu-N-C, L2 Cu-N-C, and L3 Cu-N-C. XPS survey spectrum was employed to measure the Cu content in each sample. The percentages for L1 Cu-N-C, L2 Cu-N-C, and L3 Cu-N-C were 19.0%, 23.7%, and 33.7%, respectively (Table S2.3). Out of these three samples, L2 Cu-N-C was further analyzed following acid-washing treatment. The Cu content was found to be 16.2 % in the acid-washed sample (L2/AW Cu-N-C).

The morphology of the prepared L2 Cu-N-C and L2/AW Cu-N-C samples were further analyzed by TEM. An aberration-corrected NION UltraSTEM100 was used to observe the size and distribution of individual metal atoms within the catalyst embedded in the graphene matrix. HAADF-STEM images enable the identification of Cu atoms within the graphene matrix due to the Z contrast difference. Therefore, Cu atoms, that have a higher Z value, appear as brighter spots compared to lower Z value elements such as C, N, and O. Figure 2.1 (a-d) shows both single atoms and nanoparticles in the pre-acid treated sample. In Figure 2.1(e), a line scan profile across two bright spots confirms these as single atoms with higher Z values, due to having high intense peaks. A significant number of single atoms are observed, along with randomly distributed nanoparticles ranging in size from 1.5 to 3.6 nm. The measured d-spacing of the nanoparticles corresponds approximately to Cu (111) (~0.20 nm) and Cu_2O (111) (~0.24 nm). Following acid treatment, HAADF-STEM images in Figure 2.1 (g-j) reveal the presence of single atoms. However, no nanoparticles

were observed in these samples. EDS spectra in Figure 2.2 confirm the presence of C, N, O, and Cu in the catalyst before and after acid treatment.
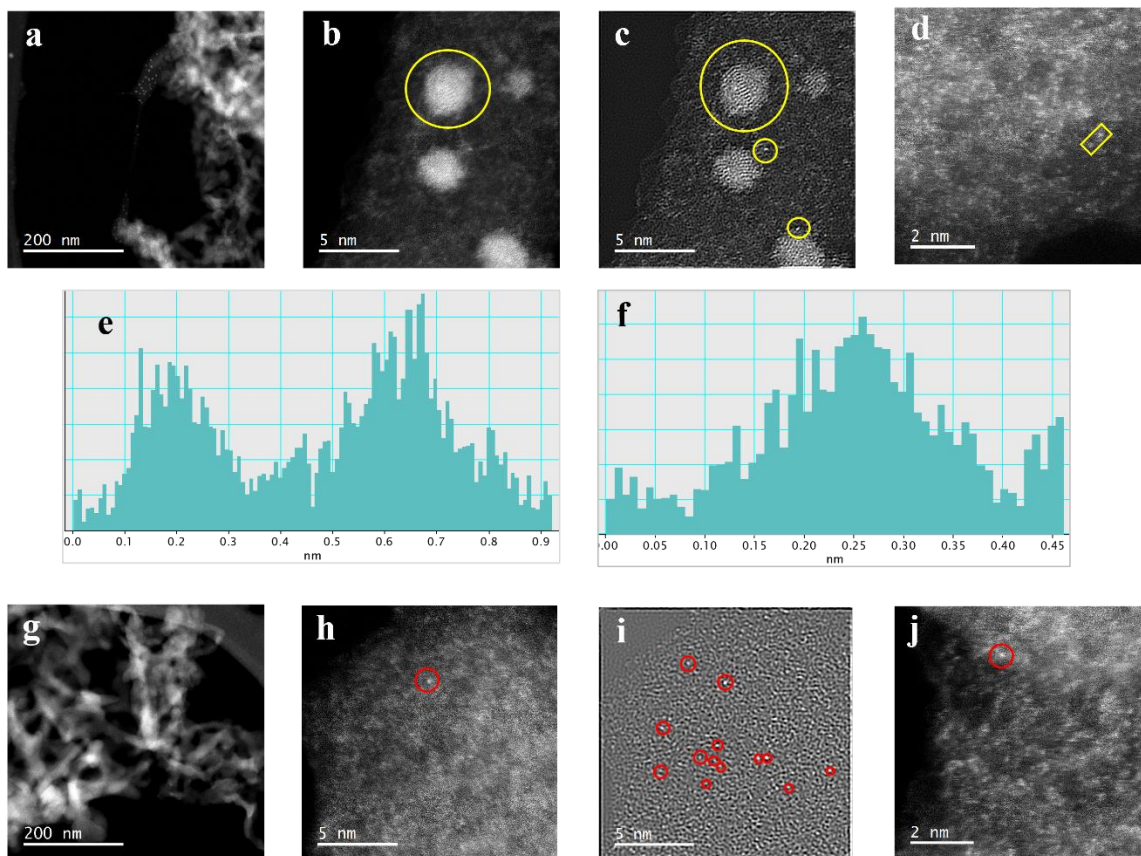
Figure 2.1: HAADF-STEM images of L2 Cu-N-C catalyst before (a-e) and after (f-j) acid wash treatment. Before acid wash images (a and b) at different magnifications. (c) IFFT filtered image of (b) showing Cu single atoms and nanoparticles (marked with yellow circles). d) at the atomic scale. (e) line scan profile across two Cu single atoms of (d) marked with a yellow rectangle showcasing their change in intensity across the line. After acid wash treatment images (g and h) at different magnifications. (i) IFFT filtered image of (h) highlighting Cu single atoms. (j) atomic scale image and (f) line scan profile across the Cu single atom of (j) marked with a red circle.
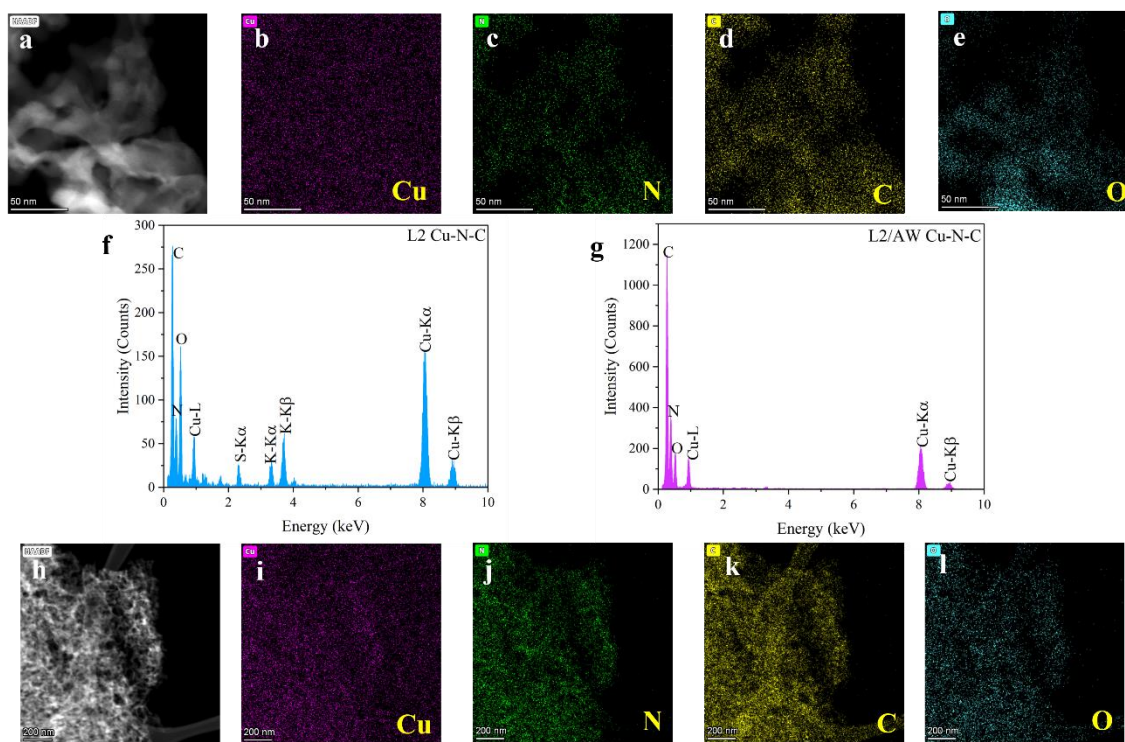
Figure 2.2: EDS mapping and the EDS spectrum showing the presence of C, N, Cu and O in the L2 Cu-N-C catalyst. (a-f) Before and (g-l) after acid washing treatment.

When comparing the EDS spectra in Fig. 2.2(f) and (g), it is evident that the amount of oxygen in the sample prior to acid washing was reduced following the acid treatment. Additionally, the presence of potassium(K), introduced during the synthesis process, was removed after the acid treatment. Hence, this purification process effectively eliminated nearly all inorganic byproducts, leaving only Cu, N, C, and O in the purified catalyst sample.

The XRD images of Fig. S2.2(a) and (b) show the XRD pattern of before-acid wash (L2 Cu-N-C) and after-acid wash (L2/AW Cu-N-C) samples. The presence of graphitic carbon, which is consistent in both the before and after acid wash samples, may account for the broad diffraction peak observed at approximately 26°. The XRD pattern shown in Figure

S2.2(a) displays three distinct peaks at 43.3°, 50.42°, and 74.14°. These peaks correspond to the (111), (200), and (220) crystallographic planes of Cu, respectively. The presence of these Cu planes confirms the existence of a pure cubic phase with a face-centered cubic (fcc) structure (JCPDS No. 85–1326). Therefore, it verifies the existence of Cu nanoparticles in the L2 Cu-N-C. However, the peaks that were missing from Fig.S2.2 (b) provided evidence of the absence of Cu nanoparticles in L2/AW Cu-N-C.[44, 45]

X-ray photoelectron spectroscopy (XPS) is employed to analyze the elemental composition and chemical states of all synthesized Cu-N-C catalysts. Figure S2.3 shows the presence of Cu, C, O, and N in the L2 Cu-N-C and L2/AW Cu-N-C samples. Notably, a prominent peak for K(potassium) is observed before the acid wash, which disappears after washing. The comparison summary of the XPS survey spectrum based on C, N, O, and Cu wt.% in all samples is given in Table S2.3. The Cu and O contents in the post-acid wash samples were decreased. This may be due to the removal of inorganic forms of Cu residues. Therefore, it demonstrates the effectiveness of our short-duration acid-leaching process in eliminating contaminants and excess unbound metal residues, thereby yielding high-purity catalysts. The deconvoluted high-resolution N1s XPS spectra of the Cu-N-C catalyst before (c) and after(f) acid washing are presented in Figure 2.3. They exhibit well-fitted peaks representing five nitrogen species, including oxidized N, graphitic N, pyrrolic-N, Cu-N, and pyridinic-N. Prior studies have confirmed that a higher pyridinic N content enhances the catalytic activity of the synthesized catalyst.[41] Moreover, an abundance of pyridinic N can serve as active sites for anchoring single Cu atoms.[46] In Figure 2.3(c), the N 1s deconvoluted spectra for the L2 Cu-N-C sample reveal peaks at binding energies (BE) of 398.0 eV (pyridinic N), 399.0 eV (Cu-N), 399.8 eV (pyrrolic N), 400.8 eV (graphitic N),

and 402.4 eV (oxidized N).[47] Similarly, Figure 2.4 (f) displays the deconvoluted N 1s spectrum for the L2/AW Cu-N-C sample. The fitting of the XPS high-resolution characteristic peaks into five prominent peaks is detailed in Table S2.4. Following the acid leaching process, the N 1s spectrum exhibits dominant pyridinic N and graphitic N peaks, which are favorable for ORR performance and serve as anchoring sites for Cu single-atom sites.[47, 48]
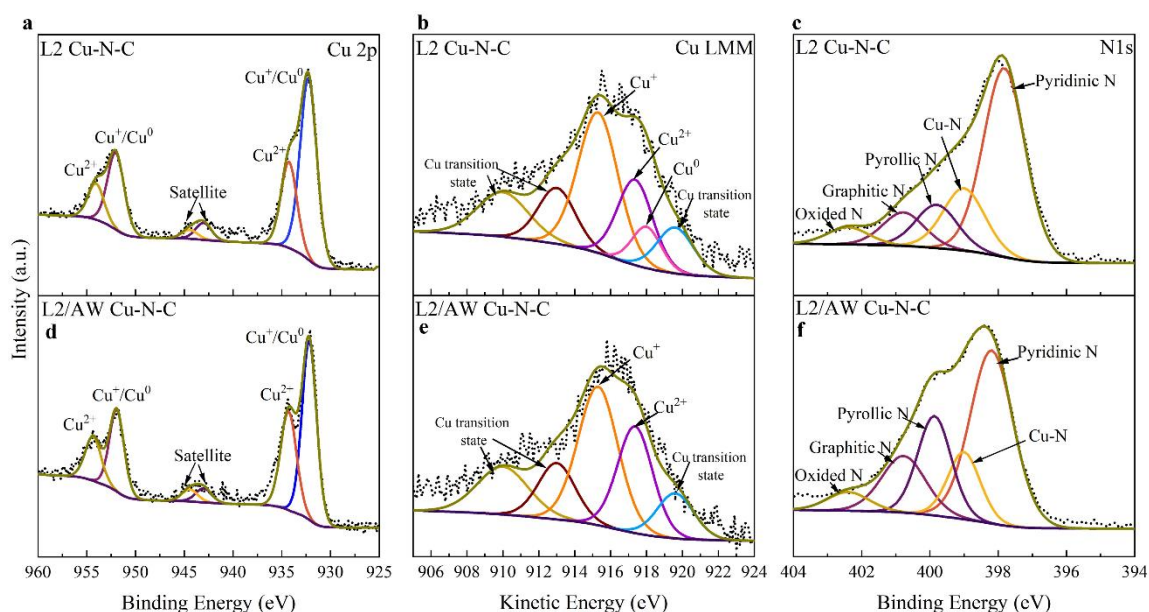
Figure 2.3: Cu 2p XPS spectra of the (a) L2 Cu-N-C and (d) L2/AW Cu-N-C after acid-washed catalyst, and Cu LMM Auger spectra of (b) L2 Cu-N-C and (e) L2/AW Cu-N-C after acid washed catalyst, and N1s XPS spectra of the (c) L2 Cu-N-C and (f) L2/AW Cu-N-C after acid washed catalyst.

Additionally, it was found that the BE of pyridinic N (398.2 eV) and pyrrolic N (399.9 eV) positively shifted to slightly higher binding energies than before the acid wash sample. Studies suggest that hydrogenation increases the coordination number of N from two to

31

three, bonded to sp2-coordinated carbon, and is expected to result in a higher BE.[49, 50] The XPS findings illustrated in Figure 2.3 depict the Cu 2p spectrum before (a) and after (d) the acid wash. Additionally, a high-resolution Cu 2p scan reveals two medium intensity peaks corresponding to Cu $2p_{3/2}$ and Cu $2p_{1/2}$ with an intensity ratio of 2:1, located within the binding energy (BE) range of 931-935 eV and 951-955 eV, respectively. The energy difference between the two prominent peaks in the Cu 2p spectrum is approximately 19.7 eV. Notably, characteristic peaks around 932.2 eV and 951.9 eV predominantly correspond to Cu^+ or Cu^0 species, while a secondary characteristic peak emerges within the range of 934–935 eV and around 954.3 eV, primarily associated with Cu^{2+} species. The peaks observed at 944.4 - 943 eV in the Cu 2p region are attributed to the satellite peak of Cu^{2+} and Cu^+.

In the analysis of the Cu 2p XPS spectrum, the closeness of binding energies for Cu^+ or Cu^0 required the utilization of the LMM Auger spectrum, as depicted in Figure 2.3 before (b) and after (e) the acid washing treatment.[51] The Cu LMM spectrum was deconvoluted into three distinct peaks: a principal peak centered around 915.3 eV, predominantly corresponding to Cu^+ species; a secondary peak at 916.9 eV attributed mainly to Cu^{2+} species; and a Cu^0 peak observed at approximately 918.0 eV. Comparing (b) and (c) spectrum it confirmed the absence of free-standing Cu metal after the acid treatment, further confirmed by HAADF-STEM results. Additionally, smaller peaks around 919.6 eV, 913.0, and 910.0 eV were due to the various Cu transition states.[52, 53] Using the Auger spectrum peak areas, the relative contents of Cu^{2+}, Cu^+, and Cu^0 species in the catalyst were determined both before and after the acid wash, as detailed in Table S2.6.

2.3.2 Electrochemical Characterization

The electrocatalytic activity for the oxygen reduction reaction (ORR) of the L1 Cu-N-C, L2 Cu-N-C, L2/AW Cu-N-C, and L3 Cu-N-C samples was evaluated using a rotating disk electrode (RDE) system with 20 wt. % Pt/C as a reference. Fig. 2.4(a) displays the linear sweep voltammetry (LSV) curves, clearly demonstrating the superior performance of the L2/AW Cu-N-C compared to all other Cu-N-C catalysts. As indicated in Fig. 2.4(b), the L2/AW Cu-N-C exhibits a half-wave potential ($E_{1/2}$) of 0.665 V vs. reversible hydrogen electrode (RHE) and a limiting current density of 6.14 mA/cm^2. Thus, this acid-washing step has been proven to further enhance the ORR activity of the L2 Cu-N-C catalyst, which had a half-wave potential ($E_{1/2}$) of 0.646 V vs. RHE and a limiting current density of 4.72 mA/cm^2. In terms of Limiting current density, L2/AW Cu-N-C shows better activity than the commercially available 20% Pt/C catalysts.
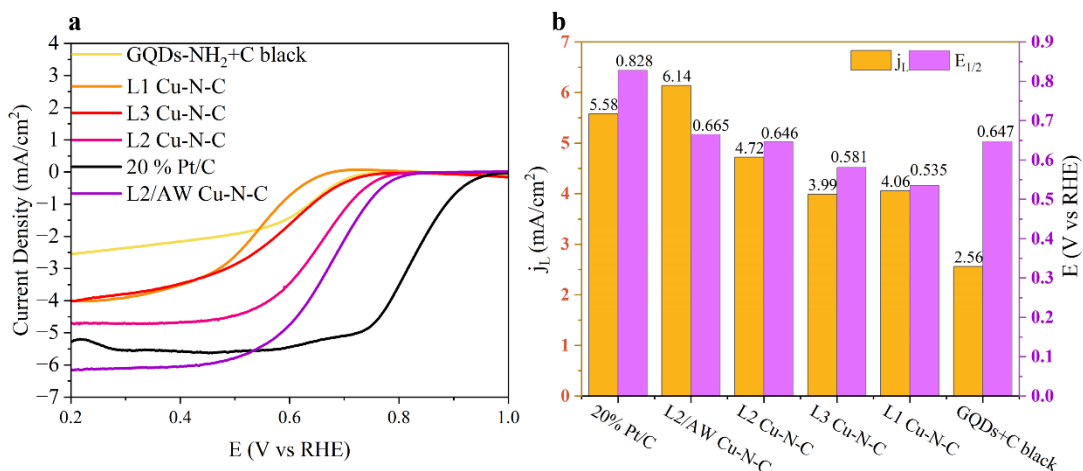
Figure 2.4: (a) ORR polarization plots of GQDs-NH$_2$ +C black, L1 Cu-N-C, L3 Cu-N-C, L2 Cu-N-C, and L2/AW Cu-N-C in 0.1 mol L^{-1} KOH solution at a scan rate of 10 mV s^{-1} and a rotation rate of 1600 rpm in comparison to that of commercial 20 % Pt/C.(b) The performance parameters of limiting current density (j$_L$) and half-wave potential ($E_{1/2}$).

The electrocatalytic ORR performance was further examined for the L2 Cu-N-C catalysts, both before and after treatment. Figure 2.5 a & b display the Cyclic voltammetry (CV) curves of the L2 Cu-N-C and L2/AW Cu-N-C obtained under N_2 and O_2 saturated electrolytes at 0 rpm. In the O_2 saturated electrolyte, both catalysts exhibit a noticeable reduction peak at 0.6 V vs. RHE, a feature absent in the N_2 saturated electrolyte, indicating the capability of the Cu-N-C for catalyzing ORR.[54]

Figure 2.5 c & d display the CV curves of the L2 Cu-N-C and L2/AW Cu-N-C obtained under N_2 and O_2 saturated electrolytes at 1600 rpm. In the N_2 saturated electrolyte, the CV curve area reflects the double-layer capacitance of the catalyst's wetted surface area. It's clear that after acid washing, the catalyst's double-layer capacitance significantly improves. Many studies have shown that acid washing enhances the pore structure and surface properties of porous carbon.[55-57] Therefore, we can propose that the increased porosity of the L2/AW Cu-N-C catalyst contributes to its enhanced double-layer capacitance.[58]
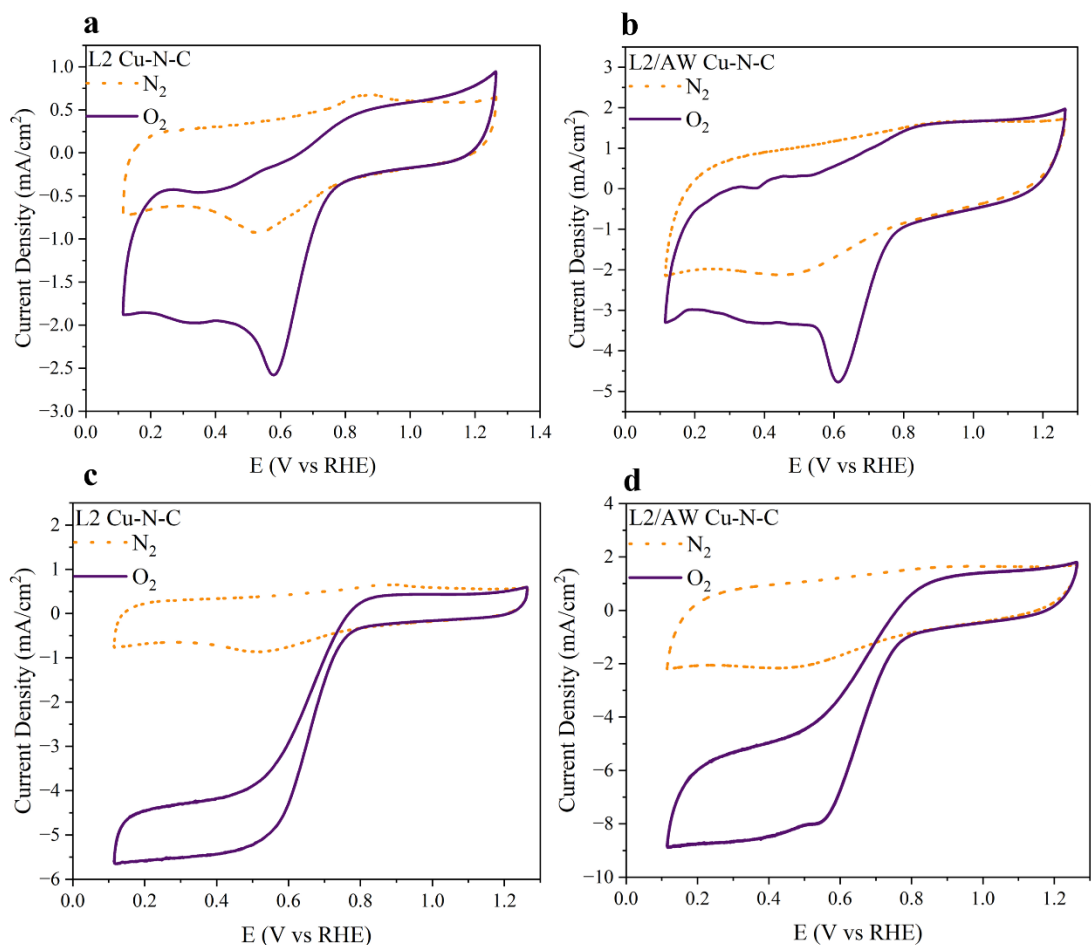
Figure 2.5: CV curve (0 rpm) of (a) L2 Cu-N-C, (b) L2/AW Cu-N-C in nitrogen or oxygen saturated 0.1 mol L^{-1} KOH solution at a scan rate of 50 mV s^{-1}. CV curve (1600 rpm) of (c) L2 Cu-N-C, (d) L2/AW Cu-N-C in nitrogen or oxygen saturated 0.1 mol L^{-1} KOH solution at a scan rate of 50 mV s^{-1}.

In experimental settings, linear sweep voltammetry conducted on a rotating disk electrode using a three-electrode system is typically employed to assess ORR performance. The half-wave potential ($E_{1/2}$), representing the potential at which half of the limiting current density from the LSV curve is reached, serves as a widely recognized metric for evaluating ORR performance. While $E_{1/2}$ is straightforward and useful, it does not effectively separate intrinsic activity from mass transfer capability, thus offering limited insight for the

35

comprehensive understanding and rational design of advanced ORR electrocatalysts.[59, 60] Therefore, investigation of the Koutecky-Levich (K-L) plot stands out as the most common method to quantify kinetic parameters and mass transfer capability of the reactants.[61] The slopes of the K-L plots enable the calculation of the number of transferred electrons (n) involved in oxygen reduction, as depicted in Figure 2.6. The n values for (c) L2 Cu-N-C and (f) L2/AW Cu-N-C were determined to be 3.5 and 4.0, respectively. These findings highlight the superior ORR activity of L2/AW Cu-N-C. The enhanced electrocatalytic activity of the acid-washed L2 Cu-N-C suggests a nearly direct four-electron transfer reaction, potentially leading to the production of water as an end product. The improved ORR activity of the optimized L2/AW Cu-N-C could be attributed to the presence of higher valence orbital energies of the ORR active atom, which enhances the adsorption of OOH* and OH* intermediates.[62]

These findings suggest that the synthesized L2/AW Cu-N-C electrocatalyst has demonstrated excellent ORR performance, with an n value of almost four, indicating the direct generation of water during the electrocatalytic process.
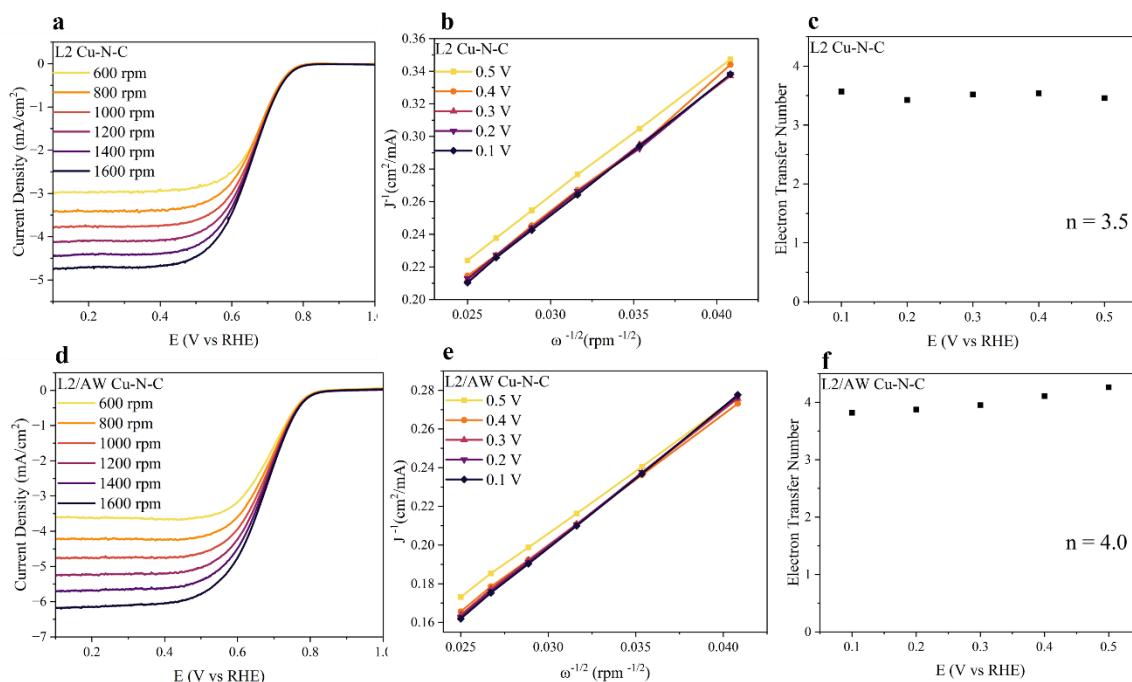
Figure 2.6: ORR Polarization plots at regular rotation rates for (a) L2 Cu-N-C, (d) L2/AW Cu-N-C with the Koutecky–Levich(K-L) plots for (b) L2 Cu-N-C,(e) L2/AW Cu-N-C and The dependence of the electron transfer number of (c) L2 Cu-N-C,(f) L2/AW Cu-N-C.

Furthermore, we carried out accelerated durability testing to further assess the ORR performance of L2/AW Cu-N-C. As shown in Figure 2.7 (a) after acid washing of the L2 Cu-N-C catalyst, a noticeable alteration in LSV curves (approximately a 40 mV negative shift) was observed before and after 250 cycles, indicating the poor durability of the catalyst.

XPS spectra were analyzed to understand how acid washing affects the catalyst's behavior in terms of its chemical state and copper content after the durability test. Table S2.9 shows the comparison of Cu wt. % of L2/AW Cu-N-C before and after use. Overall, Cu content did not change much; therefore, it confirms that there was no detachment of Cu from the

catalyst structure during the reaction. In the analysis of the Cu $2p_{3/2}$ XPS spectrum in Fig.S2.4, the curve exhibits 3 main characteristic peaks at 935 eV, 934.3 eV, and 932.3 eV. The first peak, centered around 935 eV, is primarily attributed to $Cu(OH)_2$, and the second peak at 934.3 eV is due to the presence of CuO.[63, 64] The third peak appears around 932.3 eV, mainly attributed to Cu^+ and Cu^0 species. Hence, the Cu LMM spectrum was analyzed to distinguish between Cu^+ and Cu^0 species. The main peak at approximately 915.3 eV corresponds to Cu^+, and studies found that the Auger spectrum of $Cu(OH)_2$ overlaps with Cu^+.[63, 65] Therefore, the broadening of the peak at 915.3 is due to the presence of both $Cu(OH)_2$ and Cu^+ after the durability assessment. Furthermore, Cu^0 species appear around 918.0 eV. The peak at 913.0 eV is attributed to the Cu transition states.[66]
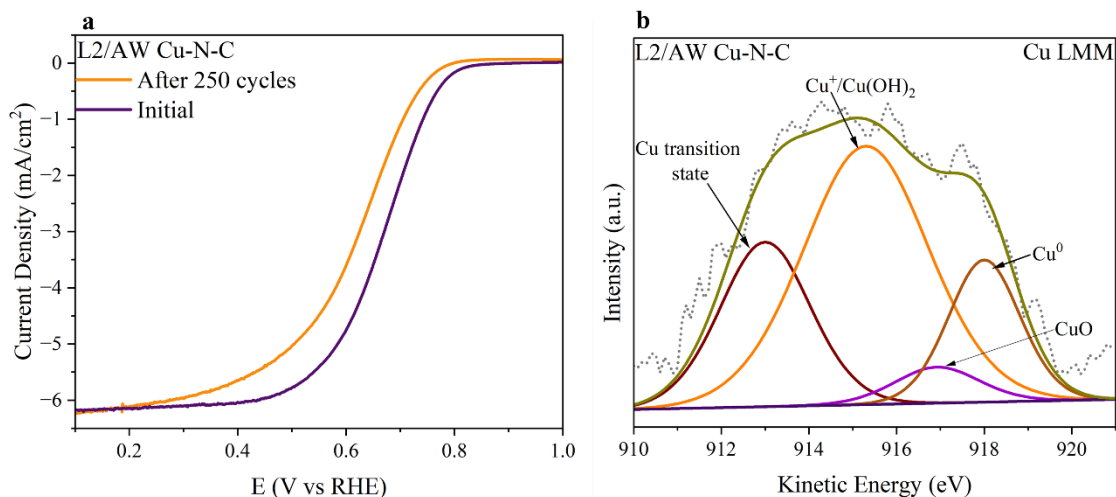
Figure 2.7: Stability testing measurements of (a) L2/AW Cu-N-C before and after 250 cycles in 0.1 mol L^{-1} KOH solution at a scan rate of 10 mV s-1 and a rotation rate of 1600 rpm. Cu LMM Auger spectra of used (b) L2/AW Cu-N-C catalyst.

Table 2.1 Summary of the Cu LMM spectrum of L2/AW Cu-N-C

Sample	Composition %		
	$Cu^+/ Cu(OH)_2$	Cu^0	Cu^{2+}
L2/AW Cu-N-C (Fresh)	35.7 (Cu^+)	0.00	24.3
L2/AW Cu-N-C (Used)	53.8 [$Cu^+/ Cu(OH)_2$]	16.7	4.8

Based on the Cu LMM peak area, the relative contents of Cu species in the catalyst before and after the durability test were calculated, as shown in Table 2.1. For the L2/AW Cu-N-fresh catalyst, the Cu^+ content was 35.7 %, Cu^{2+} was 24.3 %, and Cu^0 was absent. After the durability test, 53.8 % of Cu^+ and $Cu(OH)_2$ formed. Numerous studies have confirmed the selectivity of Cu^+ towards the reduction of oxygen through a 4-electron pathway mechanism.[54, 67] Our catalyst shows poor durability towards ORR, so we can assume it was most of $Cu(OH)_2$. A substantial increase in Cu^0 content is observed in the used catalysts compared to the fresh catalyst. Hence, it can be confirmed that the reduction of Cu^+ and Cu^{2+} to Cu^0 may contribute to the catalyst's poor durability.
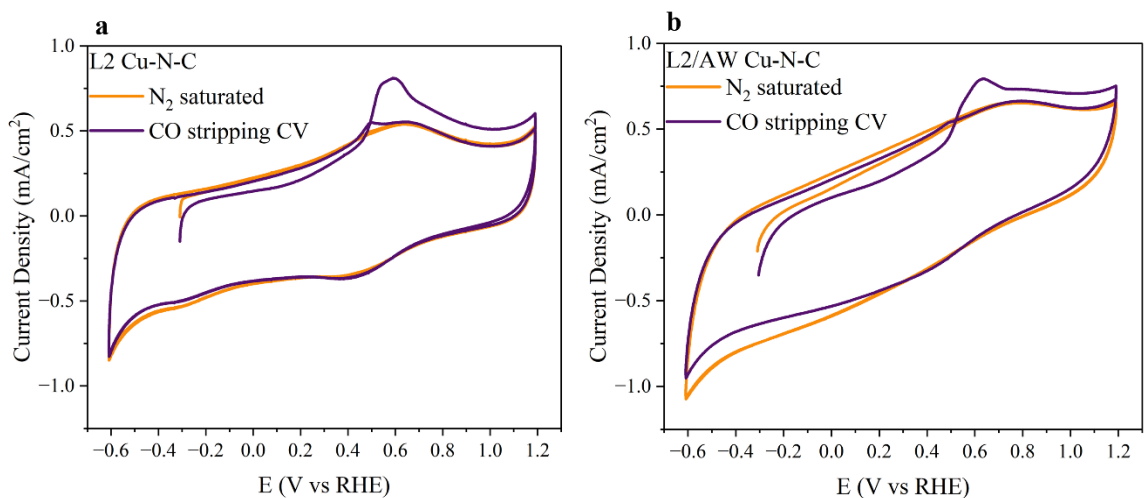
Figure 2.8: CO stripping voltammetry of (a) L2 Cu-N-C and (b) L2/AW Cu-N-C at a scan rate of 20 mVs^{-1} in 0.5 M KHCO$_3$.

In the electrochemical CO stripping experiment in an aqueous solution, CO is introduced into the cell and allowed to adsorb onto the Cu-N-C catalyst surface at a controlled potential near the thermodynamic potential, where no oxidation occurs.[36] Subsequently, CO molecules are purged to the electrolyte solution, which was already saturated with nitrogen gas. A potential sweep is then initiated, and the current response as a function of potential is recorded. Figure 2.8 shows the CO stripping experiment on (a) the L2 Cu-N-C catalyst before and (b) after acid washing, recorded using cyclic voltammetry. In Figure 2.8(a), two CO stripping peaks are observed between 0.6-1.0 V vs RHE. The lower potential peak is attributed to CO oxidation on aggregates, where the OH and CO species involved in the reaction are absorbed into different nanoparticles, indicating an inter-particle process. The higher potential peak is associated with oxidation on isolated particles, where CO and OH are absorbed on the same particle. TEM and XPS results have previously confirmed the presence of nanoparticles and single atoms in our L2 Cu-N-C sample. Figure 2.9(b) shows a single peak at a higher potential, suggesting the presence of Cu single atoms in our acid-washed sample, as confirmed by TEM and XRD results.[68]

2.4   Summary

In summary, pyrene-derived Cu-single atom catalysts were successfully synthesized with higher metal loading. This synthesis method effectively eliminates inorganic metal by-products and unbound free-standing metal nanoparticles from the Cu-N-C catalyst through a straightforward pyrolysis process followed by acid-leaching. The L2/AW Cu-N-C

exhibits improved catalytic activity towards ORR comparable to before acid-washed catalyst. The L2/AW Cu-N-C shows a Limiting current density of 6.14 mA/cm^2. Therefore, it was found that L2/AW Cu-N-C provided much higher catalytic activity towards ORR compared to the commercially available 20% Pt/C catalyst.

2.5   Supplementary Information

2.5.1   TGA analysis
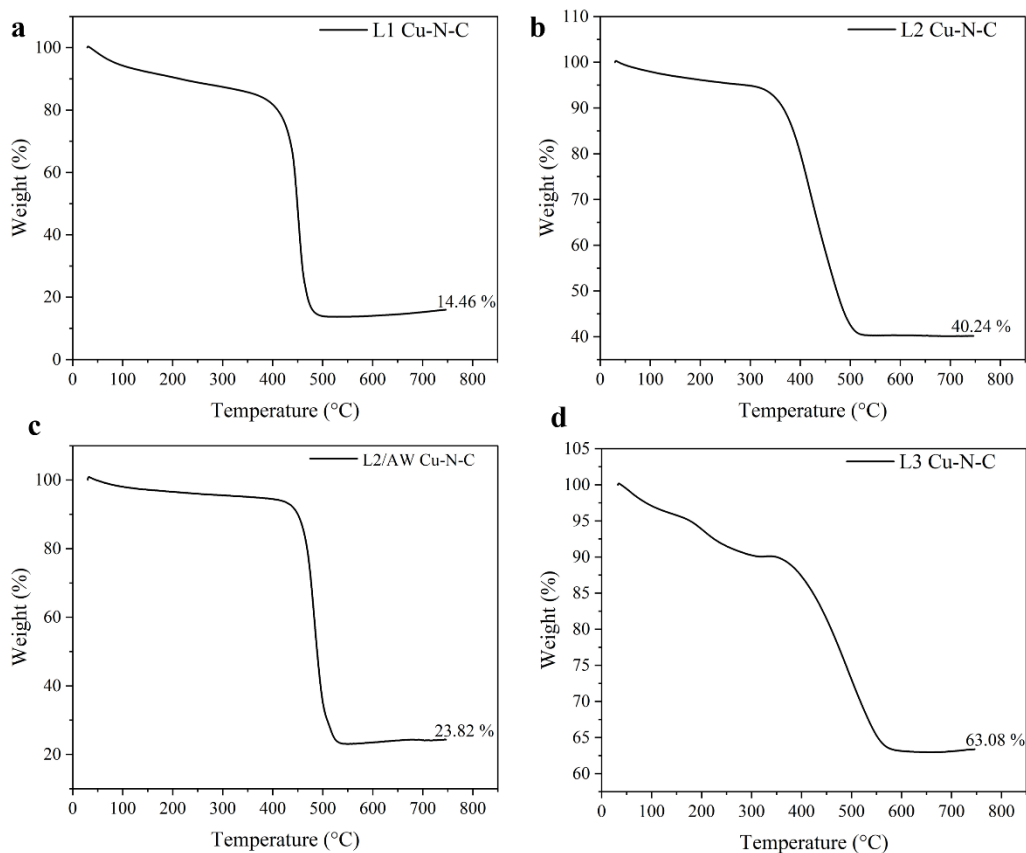
Figure S2.1: TGA thermogram of (a) L1 Cu-N-C, (b) L2 Cu-N-C, (c) L2/AW Cu-N-C and (d) L3 Cu-N-C.

Table S2. 1 Summary of the TGA analysis of all samples

.

Sample	Nominal wt%	TGA wt%
L1 Cu-N-C	15	14.46
L2 Cu-N-C	40	40.24
L2/AW Cu-N-C	40 (After acid wash)	23.82
L3 Cu-N-C	60	63.08

2.5.2 XRD analysis
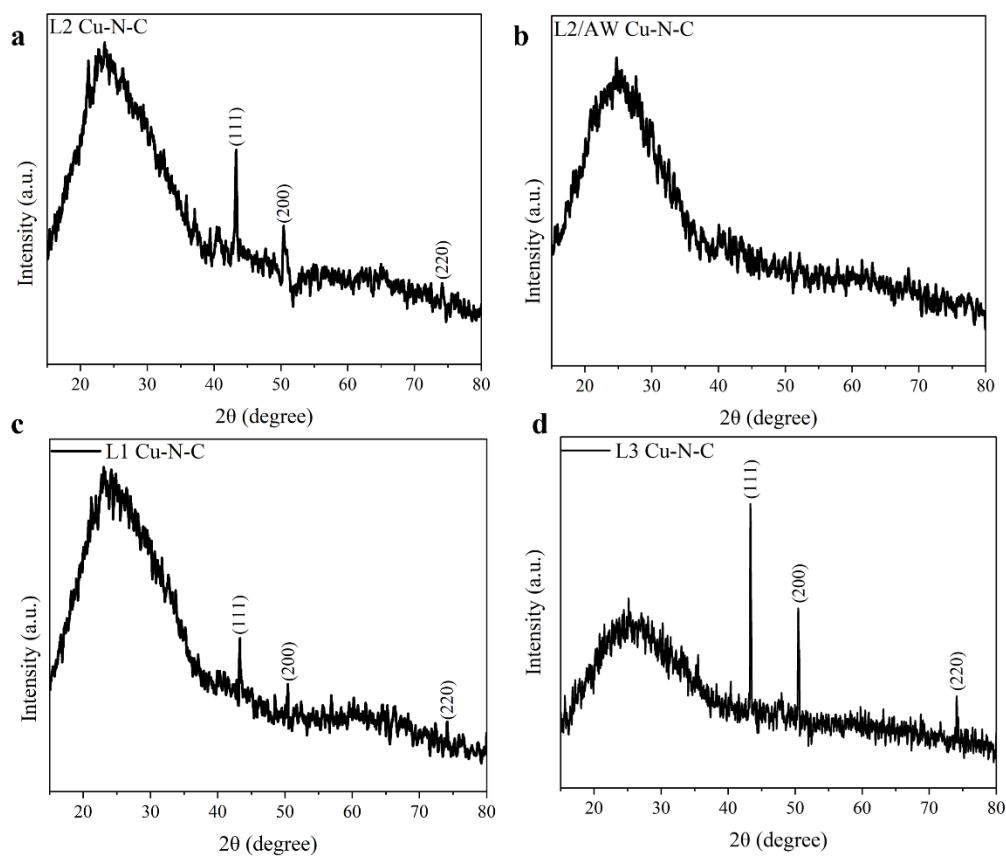
Figure S2.2: XRD pattern (a) L2 Cu-N-C, (b) L2/AW Cu-N-C, (c) L1 Cu-N-C and (d) L3 Cu-N-C.

2.5.3 XPS analysis

Table S2.2: Summary of the XPS survey analysis of all samples given as an atomic %.

Sample	C (at.%)	O (at.%)	N (at.%)	Cu (at.%)
L1 Cu-N-C	58.0 ± 0.1	13.9 ± 0.2	20.5 ± 0.1	4.9 ± 0.2
L2 Cu-N-C	56.5 ± 0.1	14.9 ± 0.1	14.2 ± 0.1	8.2 ± 0.3
L2/AW Cu-N-C	68.2 ± 0.3	9.2 ± 0.1	16.4 ± 0.3	4.6 ± 0.3
L3 Cu-N-C	58.9 ± 0.2	23.0 ± 0.3	8.2 ± 0.2	10.0 ± 0.3

Table S2.3: Summary of the XPS survey analysis of all samples given as weight %.

Sample	C (wt.%)	O (wt.%)	N (wt.%)	Cu (wt.%)
L1 Cu-N-C	42.7 ± 0.2	18.6 ± 0.3	12.6 ± 0.1	19.0 ± 0.2
L2 Cu-N-C	36.3 ± 0.3	12.8 ± 0.1	10.6 ± 0.2	23.7 ± 0.3
L2/AW Cu-N-C	53.2 ± 0.1	9.3 ± 0.1	14.6 ± 0.3	16.2 ± 0.4
L3 Cu-N-C	39.6 ± 0.2	20.5 ± 0.3	7.6 ± 0.1	33.7 ± 0.2
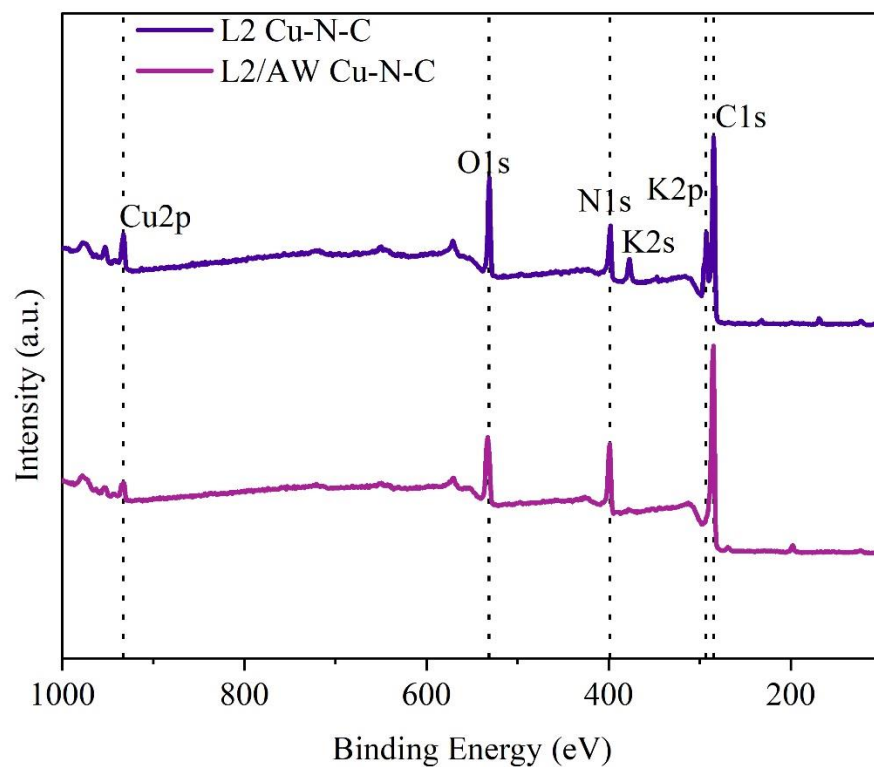
Figure S2.3:XPS survey spectrum of the L2 Cu-N-C and L2/AW Cu-N-C, catalyst respectively.

Table S2.4: XPS N 1s related chemical states in the before and after acid wash samples based on the area of the peaks.

Sample	Parameter	Oxided N	Graphitic N	Cu-N	Pyrollic N	Pyridinic N
	FWHM (eV)	1.5	1.5	1.5	1.5	1.5
L2 Cu-N-C	Peak BE(eV)	402.4	400.8	399.0	399.8	398.0
	Ratio (%)	4.9	9.8	18.0	12.6	54.6
	FWHM (eV)	1.5	1.6	1.2	1.2	1.5
L2/AW Cu-N-C	Peak BE	402.4	400.8	399.0	399.9	398.2
	Ratio (%)	4.6	15.2	13.4	20.7	46.1

Table S2.5: XPS Cu 2p related chemical states in the before and after acid wash samples based on the area of the peak.

Sample	Parameter	Cu^{2+}	Cu^+/Cu^0	Satellite	Satellite	Cu^{2+}	Cu^+/Cu^0
L2 Cu-N-C	FWHM (eV)	2.0	2.1	2.0	2.0	2.0	2.1
	Peak BE (eV)	954.3	951.9	944.4	943.0	934.3	932.2
	Ratio %	8.6	19.1	2.3	4.1	20.5	45.5
L2/AW Cu-N-C	FWHM (eV)	2.0	1.8	2.0	2.0	2.0	1.8
	Peak BE	954.3	951.9	944.4	943.0	934.3	932.2
	Ratio %	10.8	18.5	2.8	3.6	24.1	40.2

Table S2.6: Cu LMM Auger related chemical states in the before and after acid wash samples based on the area of the peak.

Sample	Parameter	Cu Transition	Cu Transition	Cu^+	Cu^{2+}	Cu^0	Cu Transition
L2 Cu-N-C	FWHM (eV)	3.5	2.5	2.7	2.4	2.0	2.5
	Peak (eV)	910.0	913.0	915.3	916.9	918.0	919.6
	Ratio (%)	14.4	13.0	35.1	19.3	7.7	10.5
L2/AW Cu-N-C	FWHM (eV)	3.5	2.5	2.7	2.4	2.0	2.5
	Peak (eV)	910.0	913.0	915.3	916.9	918.0	919.6
	Ratio (%)	15.7	13.6	35.7	24.3	0.0	10.7

Table S2.7 Cu LMM Auger related chemical states in the used acid washed sample based on the area of the peak.

Sample	Parameter	Cu Transition	$Cu^+/$ $Cu(OH)_2$	CuO	Cu^0
L2/AW Cu-N-C(used)	FWHM (eV)	2.5	2.9	2.4	2.0
	Peak (eV)	913.0	915.3	916.9	918.0
	Ratio (%)	24.7	53.8	4.8	16.7
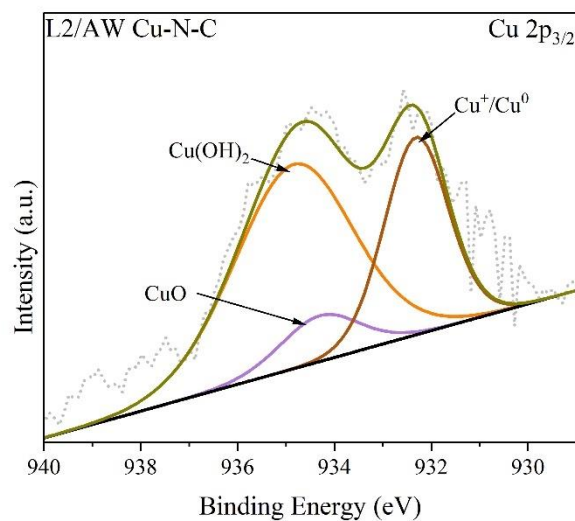
Figure S2.4: Cu 2p$_{3/2}$ XPS spectra of the used L2/AW Cu-N-C sample.

Table S2.8 XPS Cu 2p$_{3/2}$ related chemical states in the used L2/AW Cu-N-C sample based on the area of the peak.

Sample	Parameter	Cu(OH)$_2$	CuO	Cu$^+$/Cu^0
	FWHM (eV)	3.0	2.0	1.6
L2/AW Cu-N-C(Used)	Peak BE (eV)	935.0	934.3	932.3
	Ratio %	47.8	7.2	24.9

Table S2.9 Summary of the XPS survey analysis of fresh and used samples.

Sample	C (wt.%)	O (wt.%)	N (wt.%)	Cu (wt.%)
L2/AW Cu-N-C(Fresh)	53.2 ± 0.1	9.3 ± 0.1	14.6 ± 0.3	16.2 ± 0.4
L2/AW Cu-N-C(Used)	15.5 ± 0.2	19.4 ± 0.4	0.7 ± 0.2	16.9 ± 0.5
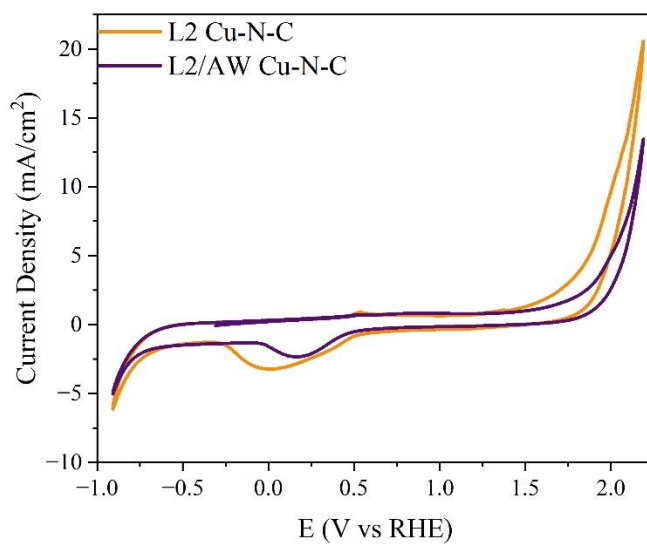
Figure S2.5: Cyclic voltammetry of L2 Cu-N-C and L2/AW Cu-N-C at a scan rate of 20 mVs^{-1} in N$_2$ saturated 0.5 M KHCO$_3$.

CHAPTER 3. CO-STRIPPING VOLTAMMETRY OF PLATINUM SINGLE ATOM
 CATALYST.

3.1   Introduction

Understanding how electrocatalysts activate single atoms or small molecules in bulk under in-situ conditions is crucial for evaluating, interpreting, and comparing their performance. The surface area of the catalyst plays a significant role in this process. Various types of areas are considered, including the geometric area, which is the flat surface area of the catalyst. The Brunauer-Emmett-Teller method (BET) is a widely used technique for quantifying the true surface area of catalysts, taking into account the porous nature of a catalyst material.[69] However, it's important to note that the BET measurement cannot pinpoint the accurate area of the catalyst that is only involved in the electrochemical reaction. It quantifies the total surface area, including both the areas that are actively involved in the reaction (active sites) and those not involved in the reaction (inactive sites). To obtain a more accurate representation of the area of the catalysts that participate in the electrochemical reaction, therefore, we turn to the method of electrochemical surface area (ECSA) measurement. ECSA is the actual area of the catalyst surface where the desired electrochemical reaction takes place.[70]But single-atom catalysts (SACs) are different from nanoparticle-based catalysts. In SACs, the isolated single atoms are anchored with heteroatoms of the support material. This unique configuration allows electrochemical reactions to occur at individual isolated sites. Consequently, in SAC analysis, the focus shifts from determining the ECSA to quantifying the site density (SD). Measuring the SD

48

provides insight into the number of active sites contributing to an electrochemical reaction.[71, 72]

The electrocatalytic reaction typically takes place at a three-phase interface involving active sites in the solid electrode, reactant gases such as O_2, CO_2, or H_2, and liquid electrolytes. This implies that only the accessible metal sites to the reactants can engage in the reaction and act as true active sites. The utilization efficiency of metal sites has not been explored widely. Specifically, in carbon support SACs, there are certain configurations of active sites that cannot be accessed by the reactants, thus not participating in catalyzing the reaction. Strategies for identifying and enhancing the utilization efficiency of single or clustered metal sites are difficult yet extremely important.[73] Currently, the ECSA of Pt group metal (PGM) catalyst is determined through underpotential hydrogen adsorption/desorption and CO stripping methods. Hence, we're exploring the capability of these techniques to measure the SD of Pt single-atom catalysts (SACs).

The determination of the ECSA through the underpotential hydrogen adsorption/desorption (HAD) reaction using cyclic voltammetry is a highly convenient method that has been successfully employed on a wide range of scales, from rotating disk electrodes (RDE) to fuel cells. Therefore, initially, we investigated the adsorption and desorption of underpotentially deposited hydrogen (H_{upd}). Applying a potential to a metal causes the adsorption of hydrogen, resulting in the formation of a monolayer on the surface with a potential less negative than the equilibrium potential of the metal. This phenomenon is known as Underpotential Deposition (UPD) and falls under the category of

pseudocapacitance.[74] Hydrogen adsorption (H_{ad}) and Hydrogen desorption (H_{de}) occur on Pt at a negative potential below 0.6 V_{RHE} (vs. RHE). The H_{upd} method can be used to calculate the ECSA under half-cell conditions; UPD of hydrogen is only known to occur on Pt group metals and at potentials positive to the hydrogen evolution reaction (HER), which occurs at 0.0 V_{RHE}. Because of this, ECSA overlaps with HER, and the resulting ECSA is always overvalued.[75] This could lead to an overestimated value of the ECSA derived from UPD.

Electrochemical CO stripping is frequently employed to determine the ECSA of catalysts based on Pt group metals (PGM) because of the strong bond that forms between CO and PGM metals. However, its use is associated with several limitations. Some of them result from an unidentified form of CO bonding on the surface. Several studies have shown that WS_2 enhances gas sensing and enables the detection of toxic gases such as CO.[76] Hence, in our study, where Pt SACs are supported on WS_2, CO oxidation may take place at both Pt active sites and WS_2. Another limitation involves accurately correcting CO stripping charges in relation to other factors such as double layer capacitance and charging from metal oxide formation. In the case of Pt SACs on a few-layered WS_2 (Pt/WS_2), this problem is significant due to the oxidation of WS_2 support overlaps with CO oxidation. CO stripping voltammetric charge determination is primarily used for qualitative purposes, with the surface area provided as a relative value rather than an absolute value. In this study, the Pt active sites in Pt/WS_2 were compared with commercial 20% Pt/C catalysts for better understanding and comparison. Furthermore, through CO stripping methods, we

confirmed that catalysts with higher loadings lead to agglomeration and the presence of single atoms and clusters in the sample, as verified by HAADF-STEM images.

3.1.1 Preparation of Pt/WS$_2$

3.1.1.1 Preparation of WS$_2$ nanosheets

By combining solvothermal and ultrasonication, a liquid-phase exfoliation-based method exfoliated the bulk WS$_2$ and broke it down into a few layered WS$_2$ nanosheets. The bulk WS$_2$ was exfoliated and broken down to a few layered WS2 nanosheets using a liquid phase exfoliation-based solvothermal and ultrasonication method. First, WS$_2$ bulk powder (0.50 g, powder, 2μm, 99%, Sigma-Aldrich) was added to a flask and degassed in a Schlenk line to remove the oxygen. Degassed ethanol: water (30% ethanol) solvent mixture (100 ml) was injected into the flask while connected to the Schlenk line. Using the probe sonicator (Sonics & Materials, Model VCX500, 12 mm probe), the resulting mixture was ultrasonicated for 1.5 hrs. Under an inert environment (in a Schlenk line), a portion of the dispersion (60–70 ml) was heated at 85 ˚C in a round-bottom flask for 6 hours. After completion of the above step, the resulting dispersion was centrifuged at 4000 rpm for 7 mins to separate the exfoliated and layered WS$_2$ nanosheets. Using a water-ethanol mixture, the separated product was washed three times to remove any impurities. The purified product was dried in the vacuum oven overnight to completely remove the solvent.

3.1.1.2 Fabrication of Pt on exfoliated WS$_2$ nanosheets

In order to obtain the desired Pt loading, various amounts of chloroplatinic acid hexahydrate were mixed with WS_2 nanosheets using a mortar and pestle to obtain a homogenous mixture. To obtain a fine layer of the mixture, the powdered sample was carefully and uniformly spread over a thoroughly cleaned shard of silicon wafer. Subsequently, it was transferred to the photonic curing device (NovaCentrix, pulseFOrge-1200 tool). The samples were produced using pulsed light with an energy density of 3.55 J/cm^2 for five milliseconds. After the photonic curing step, any unreacted chloroplatinic acid precursor was removed from the samples by washing them three times using water: ethanol solvent mixture. Two samples of Pt/WS_2 (M1 and M2) were obtained with different loadings of Pt (1.1 % and 3.3 %, respectively), and respective amounts of Pt were quantified using ICO-OES.

3.1.2 Material Characterization

The crystalline structure of all samples was analyzed using the Bruker-AXS D8 Discover diffractometer with Cu K-alpha radiation source with a wavelength of 1.5418 Å. The signal acquisition for all samples was carried out within a 2θ range of 10˚ to 90˚. The scanning rate was 0.7 deg/minute with increments of 0.02 s.

HAADF-STEM images were obtained using a Nion UltraSTEM 100 (U100) Cs-corrected electron microscope operating at 100 keV, located in the Center for Nanophase Materials Science user facility at Oak Ridge National Laboratory. The Nion U100 is a microscope that corrects aberrations up to the 5th order and has a spatial resolution of 0.1 nm. An EDS analysis was conducted using a Super-X EDS detector on an FEI Talos F200X TEM/STEM microscope operating at 200 keV, located in the same facility.

Inductively coupled plasma optical emission spectrometry (ICP-OES) was employed to quantify the amount of single-atom Pt in WS_2.

3.1.3 Electrochemical characterization

3.1.3.1 Preparation of working electrode

The catalyst ink was prepared using the following recipe for the two Pt/WS_2 samples (M1, and M2). An ink was prepared by combining 1 mg of carbon black (100 % compressed acetylene carbon black, Strem Chemicals) with 1 mg of Pt/WS_2 powder. Then 1 mL of deionized water (Barnstead™ E-pure™ ultrapure water purification system) and 20μL of Nafion (Nafion D-520 dispersion, 5% w/w in water and propanol; Beantown Chemicals) were added to the above mixture. The glassy carbon disk of the Rotating Disk Electrode (RDE) was then drop-casted with 20 μL of the catalyst ink. In total, 60 μL of the catalyst ink was drop cast onto the glassy carbon disk by repeating the previous steps twice. The geometric area of the glassy carbon disk is 0.126 cm^2. Then, the catalyst deposition was fully dried by keeping the RDE in an oven set at 60˚C. The reference catalyst was the commercial 20% Pt/C (20 wt% Pt on Vulcan CX-72, Premetek Co.). The reference 20% Pt/C catalyst ink was prepared by mixing 2 mg of 20% Pt/C with the previously mentioned volumes of Nafion and deionized water. After that, the same steps were taken to prepare the catalyst and drop cast it onto the glassy carbon disk on RDE.

3.1.3.2 Electrochemical measurements

Potentiostat (CHI 660D, CHI Instruments) was used for electrochemical measurements. The above-prepared RDE with the catalyst as the working electrode, Ag/AgCl reference electrode, and Pt wire as the counter electrode were used to perform the half-cell electrochemical measurements under acidic conditions (1.0 M H_2SO_4).

Before performing any electrochemical measurements, the electrolyte was purged and saturated with N_2 for 30 minutes. The catalyst was preconditioned by running cyclic voltammetry (CV) 20 cycles at a scan speed of 0.02 V/s within the potential range of -0.05 V to 1.25 V (vs RHE) to activate the catalyst. The potential started to scan from the initial potential to 0.3 V_{RHE} and back to 1.25 V_{RHE}. The second set of 20 CVs was recorded and utilized for ECSA calculation focusing on the H_{ad} and H_{de} regions. The CO stripping measurement involved adsorbing pure CO gas onto the working electrode at a constant potential of 0.3 V_{RHE} in a CO saturated 1.0 M H_2SO_4 electrolyte for 15 minutes using the amperometric i-t curve function. Then N_2 gas was purged for an additional hour to remove any unbound CO gas molecules from the electrolyte completely. After that, CO stripping CVs were recorded at a scan rate of 0.02 V/s within the same potential range. The following formula was used in all measurements to convert the potential values measured with regard to the Ag/AgCl to the Reversible Hydrogen Electrode (RHE):

$V_{RHE} = V_{Ag/AgCl} + 0.222 + 0.059 \times pH_{electrolyte}$

The ECSA was calculated using the following formula.

$$Q[C] = \frac{A\,[AV]}{S\,[V/s]} \quad [eq.1] \qquad\qquad ECSA[m^2/= \frac{Q[C]}{\Theta f[C/m^2]m_{metal}[g]} \quad [eq.2]$$

First Q, the total charge was determined by equation 1, where A is the total area derived from CO stripping or Hupd on Pt active sites, and S denotes the scan rate. Assuming a complete monolayer coverage of the catalyst $\Theta = 1$, the conversion factor f =420 μCcm^{-2} for CO stripping or 210 μCcm^{-2} for H_{upd}. The metal loading (m_{meta}) is calculated based on the absolute amount of metal drop cast on the RDE.[75]

The SD was calculated using the following formula.

$$Q_{CO\ strip}[C/g] = \frac{A[AV]}{S[V/s]\times Absolute\ metal\ loading[g]} \quad [eq.3]$$

$Q_{\text{co strip}}$ is the CO striping charge calculated from equation 3, where A is the total area derived from CO stripping on Pt active sites, and S denotes the scan rate.

$$SD\ [sites/g]\ =\ \frac{Q_{CO\ strip}[C/g] \times N_A[mol^{-1}]}{n_{CO\ strip} \times F[C/mol]}\ [eq.4]$$

Site density (SD) was determined using equation 4, where N_A stands for Avogadro number, F stands for Faraday constant, and n CO strip is the number of electrons participating in the oxidation of CO adsorbed on the metal center.[72]

3.2   Results & Discussion

3.2.1   Material characterization

Powder X-ray diffraction was used to investigate the crystalline structure and phase composition of the synthesized samples. As shown in Fig. S3.1, the XRD spectra for all two loadings were compared with commercial 20% Pt/C. The peaks are attributed to the (002), (004), (006), and (008) planes of WS_2 (JCPDS No.08-0237). In all Pt/WS_2, there isn't a distinctive Pt nanoparticle-related diffraction peak (JCPDS no.: 04-0802 Pt). Therefore, it verifies the presence of single Pt atom species on WS_2 nanosheets.
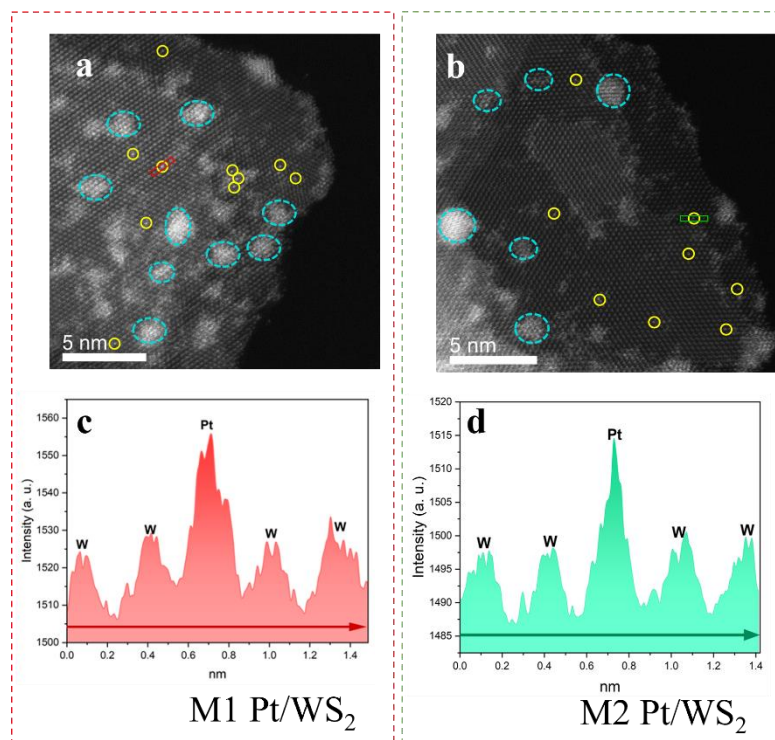
Figure 3.1: HAADF-STEM images of Pt/WS$_2$ samples. Yellow circles represent individual Pt atoms, while blue dashed circles represent Pt clusters (a) M1 Pt/WS$_2$, (b) M2 Pt/WS$_2$. Intensity profiles indicate greater intensity for Pt compared to W atoms (c) M1 Pt/WS$_2$, (d) M2 Pt/WS$_2$.

Aberration-corrected HAADF-STEM images can detect Pt atoms in WS$_2$ using the differences in Z contrast. Pt atoms, with their higher Z number, are visible as bright spots on the WS$_2$ nanosheets, as shown in Figure 3.1(a-b). Intensity profiles demonstrate variations in intensity across multiple bright spots in all samples (Fig. 3.1(c-d)), with Pt atoms exhibiting higher intensity attributed to their higher Z value. The yellow circles represent individual Pt atoms, while the blue circles represent Pt clusters, showing the presence of both Pt single atoms and Pt clusters in all two samples. Figure S3.2 (a) shows pristine few layered WS$_2$ nanosheets, while their intensity profile in Figure S3.2 (b)

indicates a similar intensity within the orange rectangle, indicating the presence of W atoms. The energy-dispersive spectroscopy (EDS) element mapping, coupled with scanning transmission electron microscopy (STEM), illustrates the uneven distribution of atomic Pt across the Pt/WS2 samples (Fig. 3.2 a-b). Furthermore, EDS mapping and spectra (Fig. 3.2 c-d) confirmed the presence of Pt in all two samples.
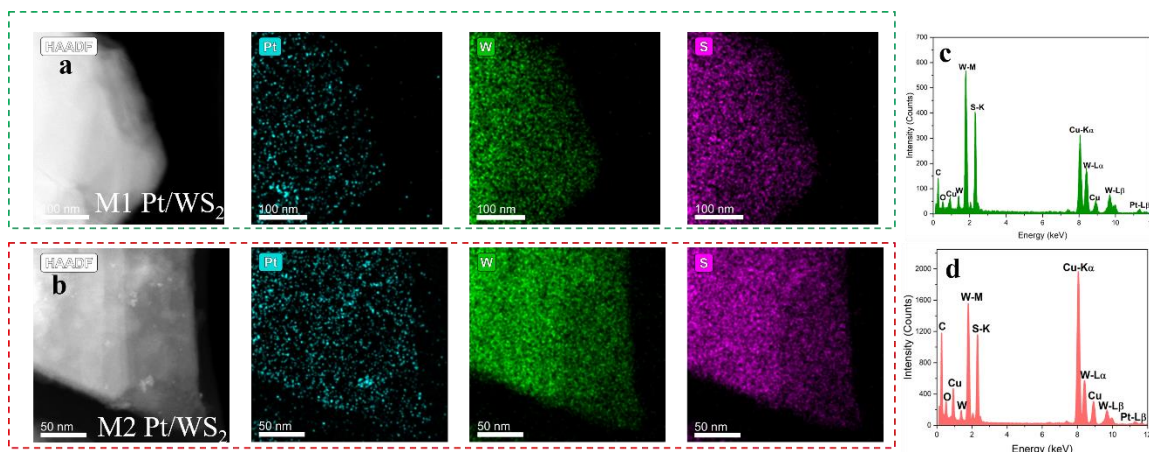
Figure 3.2: STEM images and their respective EDS elemental mappings (a) M1 Pt/WS$_2$, (b) M2 Pt/WS$_2$, and EDS spectrum, (c) M1 Pt/WS$_2$, (d) M2 Pt/WS$_2$.

3.2.2 Electrochemical Characterization

3.2.2.1 Hydrogen adsorption method

The electrochemical profiles of Pt/WS$_2$ electrocatalysts in 1.0 M H$_2$SO$_4$ were qualitatively evaluated to determine the applicability of the selected methods to measure ECSA in RDE setups. Figure S3.4 displays the cyclic voltammograms of two Pt/WS$_2$ and WS$_2$ catalysts in an N$_2$ atmosphere, along with the stripping voltammetry of adsorbed CO in 1.0 M H$_2$SO$_4$. All the cyclic voltammetry experiments were conducted within the voltage range of -0.05 V to 1.4 V(RHE). A notable oxidation peak of WS$_2$ was observed after 1.2 V$_{RHE}$.

The CO stripping peak for all Pt/WS$_2$ catalysts was around 1.2 V$_{RHE}$. Therefore, to prevent interference from the significant oxidation of the WS$_2$ support, the potential range was reduced to 1.25 V$_{RHE}$.

Initially, the underpotentially deposited hydrogen adsorption and desorption method was used to calculate the total number of electrochemically reactive surface sites on Pt/WS$_2$, with commercial 20% Pt/C being used as a reference. The technique, which is widely known, is based on calculating the charge required to remove an adsorbed hydrogen monolayer.[75] This is essentially accomplished by integrating the current in the cathodic or anodic scan of the H$_{ad}$/H$_{de}$ region shown in Fig. S3.5.

In Figure 3.5(a), the total charge of H$_{ad}$ is noticeably higher than the total charge of H$_{de}$ areas for all Pt/WS$_2$ catalysts and pristine WS$_2$ support. However, for 20% Pt/C, the total charges due to H$_{ad}$ and H$_{de}$ are quite similar. This similarity arises because hydrogen forms a monolayer on the 20% Pt/C, leading to the desorption of all adsorbed hydrogen. In Pt/WS$_2$, the WS$_2$ support consists of a few layers, as shown in previous high-resolution STEM images (Figure S3.2 a). Thus, it is reasonable to assume that hydrogen adsorbs not only on the surface of the catalyst but also between the layers of WS$_2$. Consequently, not all adsorbed hydrogen is desorbed from the Pt/WS$_2$ catalyst. When the ECSA of the Pt/WS$_2$ catalyst was calculated using the H$_{ad}$ and H$_{de}$ areas, significantly higher values were obtained compared to 20% Pt/C. Furthermore, this suggests that the hydrogen is not only adsorbed onto the Pt species on WS$_2$ support but also onto the WS$_2$ and in between the layers. Therefore, for Pt/WS$_2$ catalysts, we only consider the total charge resulting from hydrogen adsorption and desorption.

Figure 3.3(d) displays the H_{de} on 20% Pt/C, revealing multiple peaks, such as Pt(100) and Pt(110). These peaks result from the crystalline structure of the surface planes in Pt nanoparticles, which is absent in Pt/WS$_2$.[77]
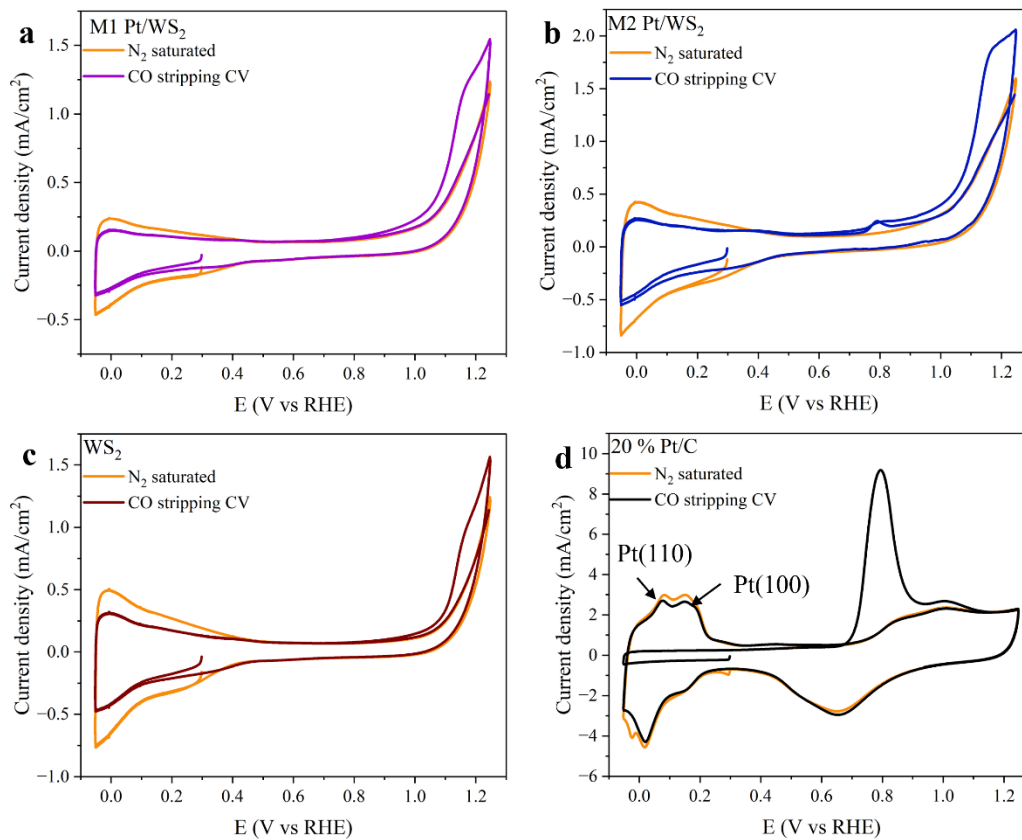
Figure 3.3: Cyclic voltammograms of H_{upd} recorded during N$_2$ saturation and CO stripping of (a) M1 Pt/WS$_2$, (b) M2 Pt/WS$_2$, (c) WS$_2$, and (d) 20% Pt/C at a scan rate of 20 mV/s in 1.0 M H$_2$SO$_4$.

3.2.2.2 CO stripping method

The CO stripping experiment was conducted for different time durations, and we found complete CO coverage was attained on 20% Pt/C after 15 minutes. Figure 3.3(d)

demonstrates that the 20% Pt/C surface has been completely saturated with adsorbed CO, as indicated by the complete blockage of pseudocapacitive currents in the potential range below 0.4 V.[78]

The CO stripping CV in Figure 3.3(d) shows that the CO adsorbed layer recovers after complete stripping off from the 20% Pt/C. The region H_{ad}, and H_{de} takes place, overlapping with the CV curve (in yellow) obtained for underpotential H_{ad} and H_{de}. This suggests that on the carbon support of 20 wt% Pt, the H and CO adsorption sites are the same. However, even after CO has been adsorbed on all Pt/WS2 catalysts (M1 and M2), Figure 3.3 (a-b) shows the existence of pseudocapacitive current in the potential range below 0.4 V. Furthermore, Figures 3.3 (a–b) show that the pseudocapacitance region did not recover even after the CO on Pt/WS_2 was completely oxidized. This suggests that in Pt/WS_2, the CO adsorption sites are not similar to underpotential H adsorption sites. This phenomenon can be attributed to the hydrogen spillover effect on Pt/WS_2 catalysts. It involves activated H atoms migrating from metal particles rich in Hydroden to a support surface lacking hydrogen.[79]

An interesting relationship can be observed in Figure 3.4(f) when comparing the CO stripping curve of 20% Pt/C with that in Figure 3.4(d). Both samples exhibit a distinct single peak at 0.8 V_{RHE}, attributed to the existence of Pt nanoparticles or clusters. Previous studies have found CO oxidation occurs at a significantly higher potential on isolated particles.[68] Therefore, M2 Pt/WS_2 seems to have two primary different types of CO oxidation sites. Figure 3.4 (e-f) indicates that a greater amount of CO oxidation occurred

at potentials higher than 0.8 V, suggesting the existence of isolated Pt atoms on all Pt/WS$_2$ catalysts, as confirmed by HAADF-STEM images.
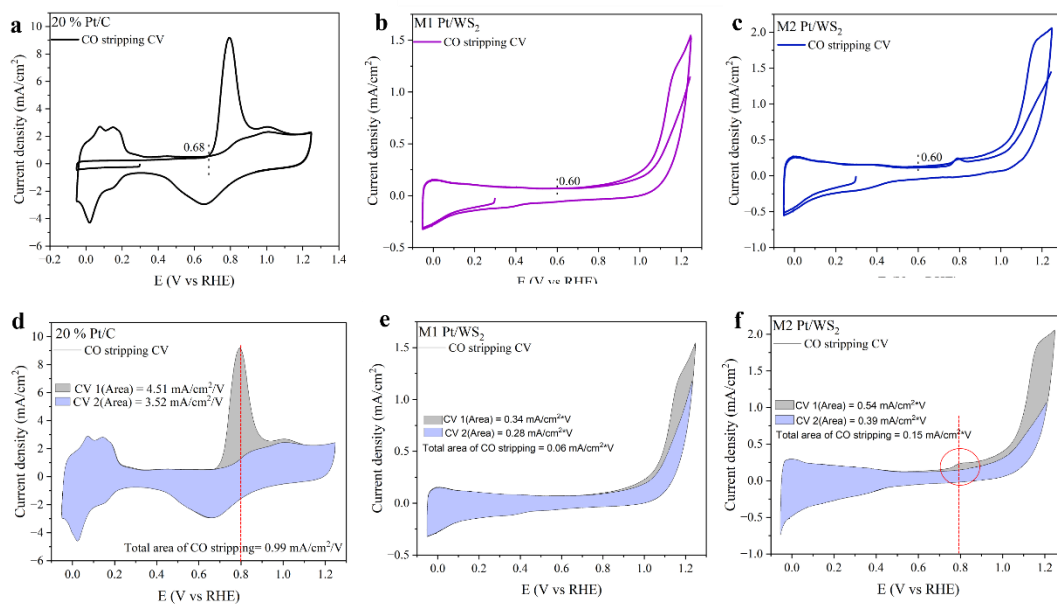
Figure 3.4: CO-stripping cyclic voltammograms for (a) 20% Pt/C, (b) M1 Pt/WS$_2$, (c) M2 Pt/WS$_2$, and their CO oxidation potentials are shown by the black dashed lines. CV cycles shaded in ash color show the CO stripping, and those shaded in blue represent the second CV curve following the oxidation of surface-bound CO for (d) 20% Pt/C, (e) M1 Pt/WS$_2$, and (f) M2 Pt/WS$_2$ at a scan rate of 20 mV/s in 1.0 M H$_2$SO$_4$.

The CO stripping areas in Pt/WS$_2$ were corrected for capacitive current, CO adsorption on the WS$_2$ support, and surface oxidation at high potential. Hence, the area of the first CO stripping curve was subtracted from the area of the second CV curve and from the CO adsorption area obtained for WS$_2$. Consequently, the SD derived from this method represents the electrochemically active Pt sites of the Pt/WS$_2$ catalysts. Figure 3.5 (b) illustrates the SD of all Pt/WS$_2$ catalysts obtained from the CO stripping method.

61

Calculations show that M2 Pt/WS$_2$ exhibits a higher SD than M1 Pt/WS$_2$. Therefore, we can suggest that the higher Pt wt%, the M2 Pt/WS$_2$ catalyst has a greater SD due to the presence of more single atoms compared to M1 Pt/WS$_2$.
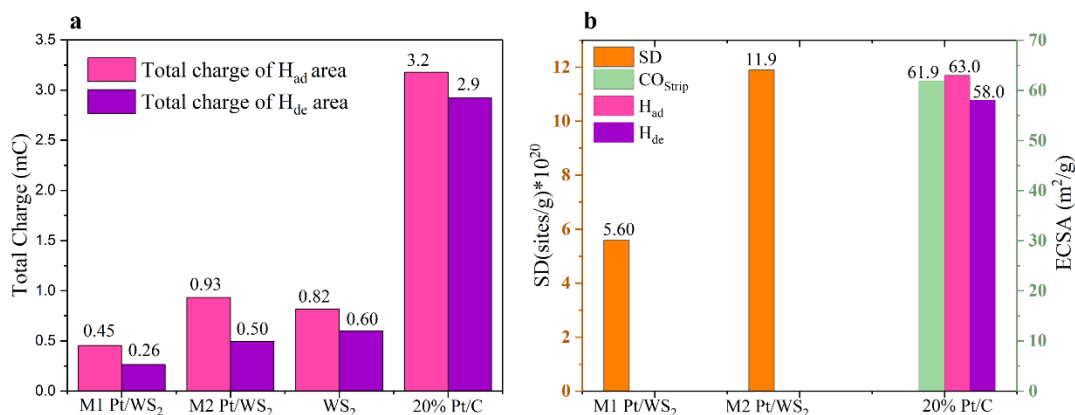
Figure 3.5: (a) Total charge of H$_{ad}$, and H$_{de}$ area of M1 Pt/WS$_2$, M2 Pt/WS$_2$, WS$_2$ and 20% Pt/C, (b) SD derived from CO stripping for M1 Pt/WS$_2$, M2 Pt/WS$_{2,}$ and ECSA derived from CO stripping, H$_{ad}$, and H$_{de}$ methods for 20% Pt/C.

3.3 Summary

This study highlights the significant role of CO stripping voltammetry in assessing the SD of Pt-SACs. Our findings reveal a correlation between CO stripping peaks and the smaller particle size Pt exhibit CO stripping at higher potentials, while larger particles show CO stripping at lower potentials. Remarkably, M2 Pt/WS$_2$ demonstrates a greater SD. In order to identify exclusively the Pt sites that are electrochemically active, a baseline subtraction was carried out based on the assumption that the processes of metal oxidation formation and double-layer capacitance are the same. Subsequently, the baseline-corrected CO

stripping areas were further adjusted by subtracting the CO stripping area attributed to WS$_2$, resulting in SD values solely associated with Pt active sites.

3.4   Supplementary Information
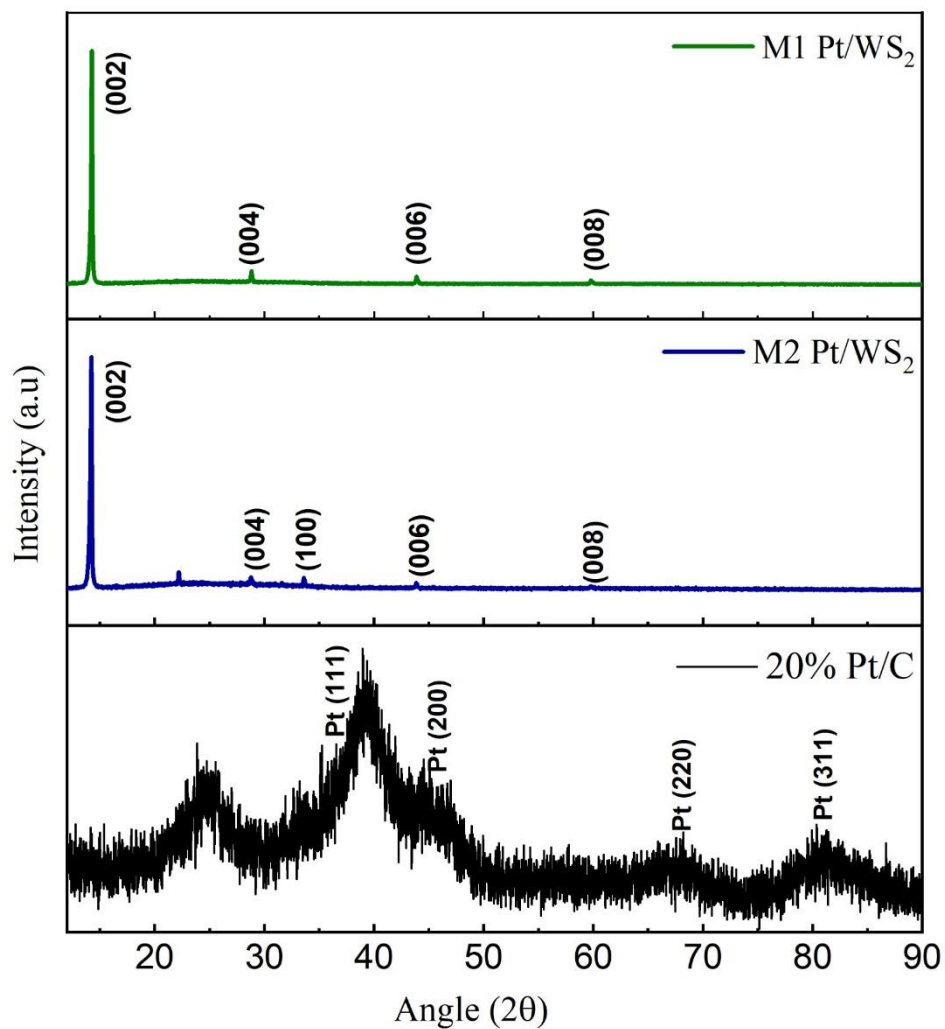
Figure S3.1: XRD patterns of the M1 Pt/WS$_2$, M2 Pt/WS$_2$ and commercial 20% Pt/C.
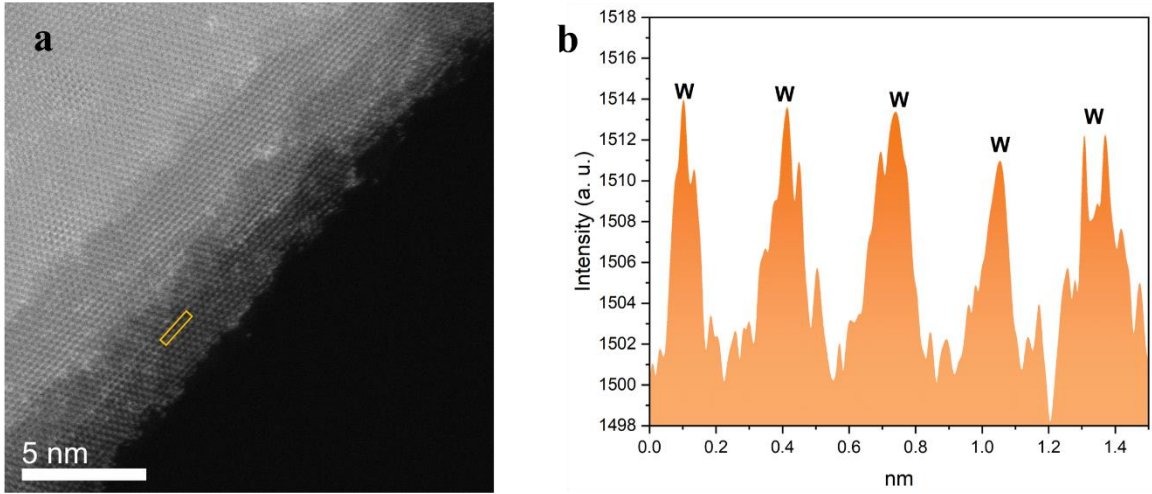
Figure S3.2: (a) HAADF-STEM images of pristine WS$_2$. (b)Intensity profiles indicate changes in intensity across the orange rectangle marked in (a).
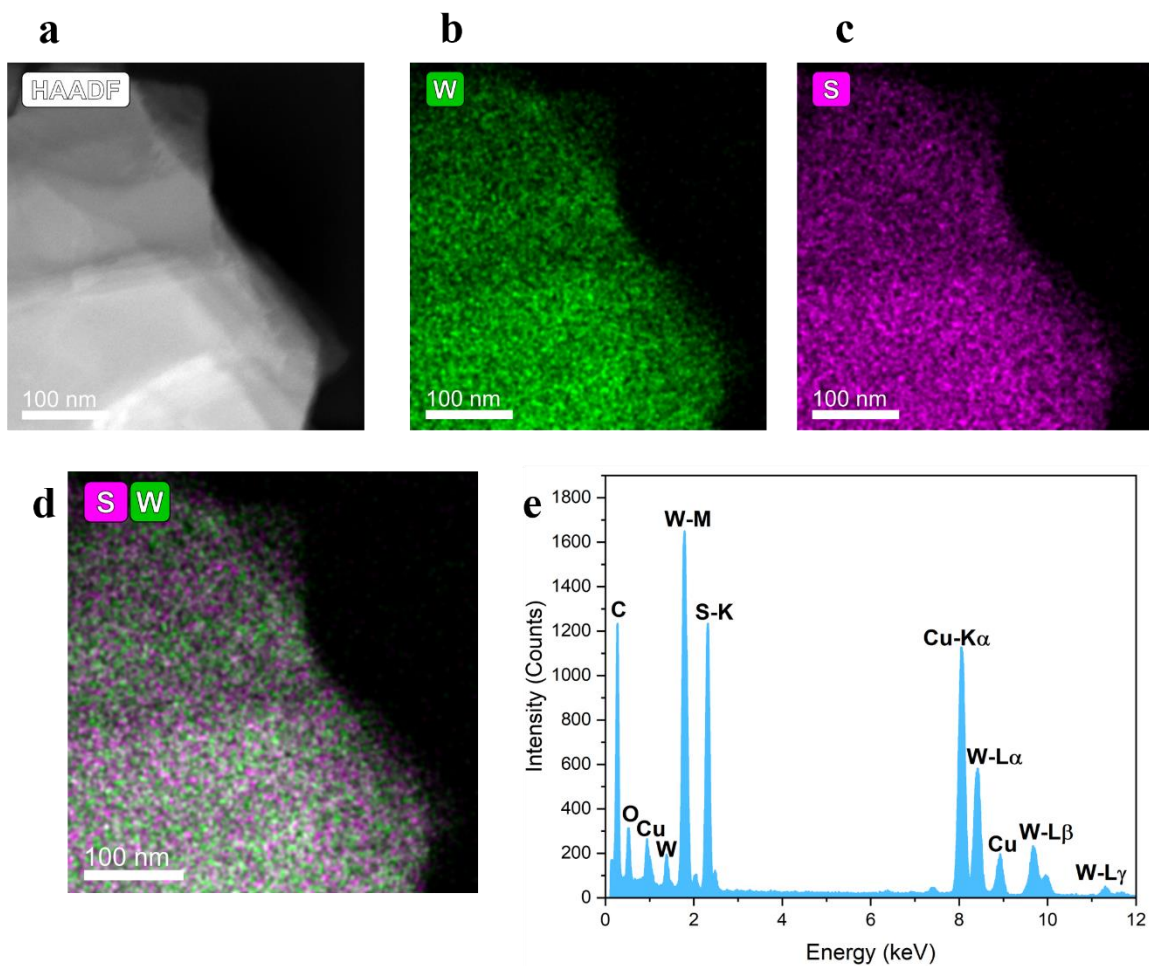
Figure S3.3: (a)STEM image, (b-d) their respective EDS elemental mappings, and (d) EDS spectrum of pristine WS$_2$.
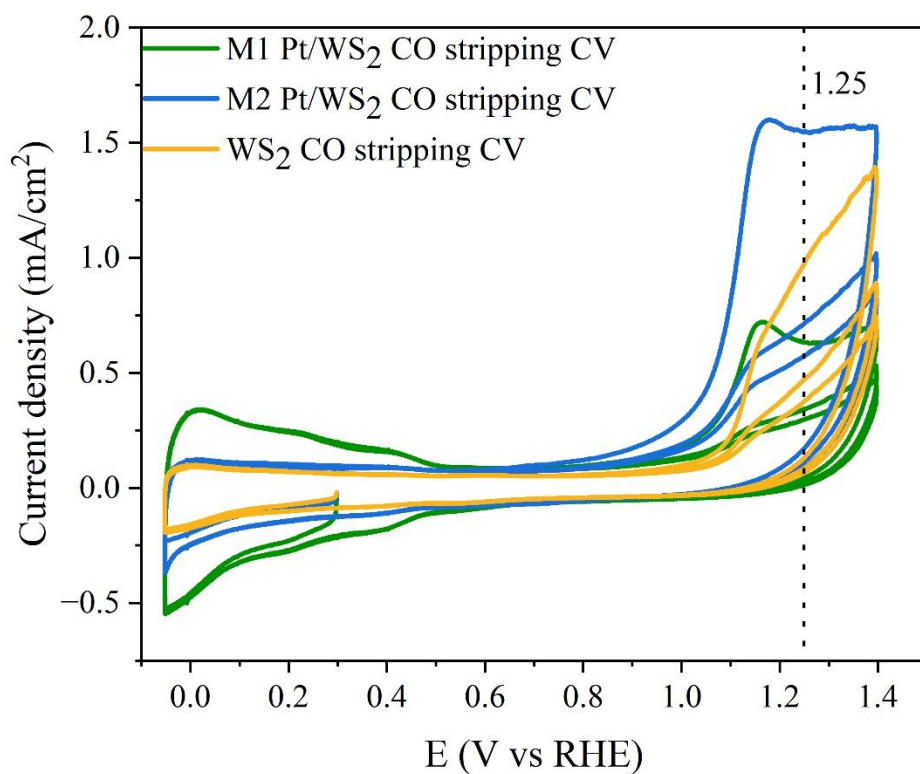
Figure S3.4: Overlaid cyclic voltammograms of CO stripping for M1 Pt/WS$_2$, M2 Pt/WS$_2$ and WS$_2$ at a scan rate of 20 mV/s in 1.0 M H$_2$SO$_4$, covering a wide potential range where oxidation of WS$_2$ occurs after 1.25 V$_{RHE}$.
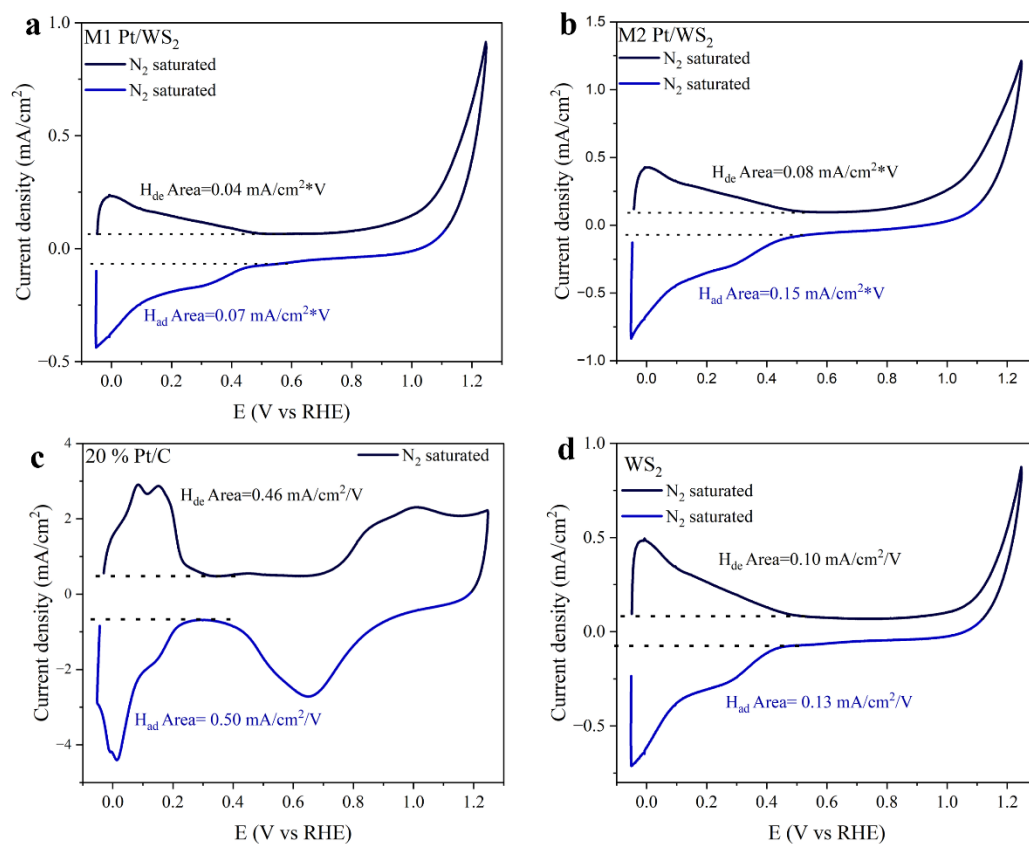
Figure S3.5: Cyclic voltammograms of H_{upd} recorded during N_2 saturation (a) M1 Pt/WS$_2$, (b) M2 Pt/WS$_2$, (c) 20% Pt/C, (d) WS$_2$, at a scan rate of 20 mV/s in 1.0 M H$_2$SO$_4$. Dashed lines represent the background current density as a baseline for determining the areas of H_{ad} and H_{de}.
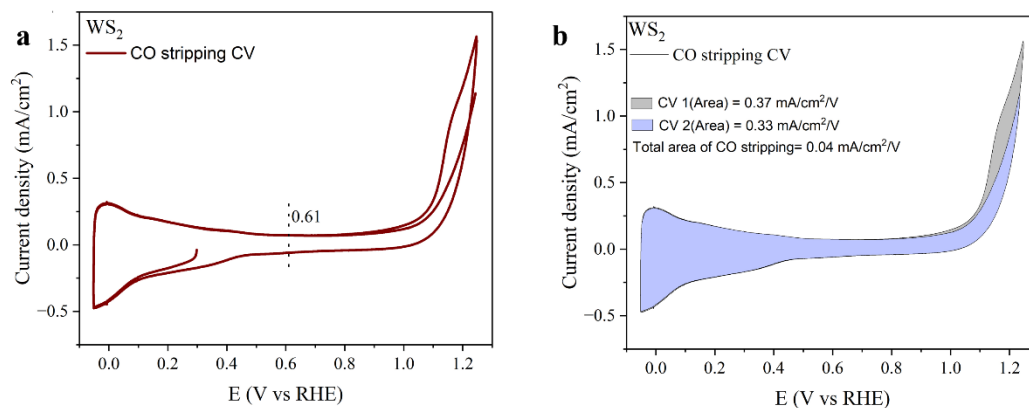
Figure S3.6: CO-stripping cyclic voltammograms for (a) WS_2 and its CO oxidation potential is shown by the black dashed line. On the right side, CV cycles shaded in ash color show the CO stripping and those shaded in blue represent the second CV curve following the oxidation of surface-bound CO for (b) WS_2 at a scan rate of 20 mV/s in 1.0 M H_2SO_4.

CHAPTER 4. CONCLUSION AND FUTURE DIRECTIONS

This dissertation begins by explaining the significance and fundamental background of ORR, single-atom catalysts, and CO stripping methods. Today, fuel cells have gained significant attention due to their ability to directly convert chemical energy into electric energy without using fossil fuels. The cathodic reaction, ORR, in fuel cells with sluggish kinetics is the primary factor that limits fuel cell performance. PGM catalysts are used to overcome these limitations. But their higher cost, less abundance, and poor durability efforts have been made to replace Pt. The non-PGM-based ORR electrocatalysts emerged as promising alternatives to Pt due to their abundance, cost-effectiveness, performance, and stability. One of the promising approaches is transition metal doped−nitrogen−carbon (M-N-C) catalysts, which are cost-effective and efficient in applications like fuel cells, particularly for the ORR. This thesis reports the detailed study of Cu-N-C as an excellent electrocatalysis for ORR. This thesis also covers the in-situ quantification method of electrochemically active sites of Pt-based SACs.

Chapter 2 presents a straightforward pyrolysis protocol followed by acid leaching to synthesize a non-PGM-based single-atom catalyst with higher metal loading. High-resolution STEM images confirmed the removal of Cu nanoparticles present in L2 Cu-N-C. EDS spectra and the XPS survey spectrum of L2/AW Cu-N-C confirmed the effective elimination of all inorganic byproducts after the acid leaching. L2/AW Cu-N-C showed excellent electrochemical performance towards ORR compared to before acid washed sample. Also, L2/AW Cu-N-C shows a higher limiting current density compared to

commercially available 20 %Pt/C catalysts. Therefore, this synthesis procedure can be successfully applicable for obtaining Cu-SACs with higher metal loading with enhanced ORR activity.

This work can be extended by improving the durability of L2/AW Cu-N-C in working conditions. When comparing fresh L2/AW Cu-N-C with the used catalyst, we found that the formation of Cu^0 was due to the reduction of Cu^{2+} and Cu^+. The pyrolysis step can be adjusted with higher temperatures to strongly anchor the metal precursors to the N-doped carbon structure. Density function theory (DFT) calculations, along with computational studies, can be carried out to get a better understanding of the reaction mechanisms for further improving the catalytic activity.

Chapter 3 focused on determining the site density (SD) of a Pt-based single-atom catalyst using the CO stripping method. High-resolution STEM images confirmed the presence of both Pt single atoms and Pt clusters in all two samples. Furthermore, high-resolution STEM images confirmed the pristine few layered WS_2 nanosheets as the support material. CO oxidation takes place in both Pt active sites and a few layered WS_2 nanosheets. M2 Pt/WS_2 seems to have two primary different types of CO oxidation sites compared to 20%Pt/C. CO absorbs Pt nanoparticles oxidized at 0.8 V (vs. RHE). The oxidation of CO adsorbs to Pt single atoms occurred at potentials higher than 0.8 V (vs. RHE). M2 Pt/WS_2 with higher Pt loading has higher SD due to the presence of a higher number of electrochemically active sites.

Future studies can be carried out to obtain an accurate number of electrochemical active sites using the CO stripping method, linked with other confirmation experiments. We can use diffuse reflectance infrared Fourier transform spectroscopy (DRIFTS) with CO as a probe molecule to Pt/WS$_2$ catalysts to investigate in detail the nature of the active Pt sites. Differential Electrochemical Mass Spectrometry (DEMS) can be used to combine electrochemical half-cell experimentation with mass spectrometry further to confirm the accurate number of Pt single atoms. In situ, attenuated total reflection surface-enhanced infrared absorption spectroscopy (ATR-SEIRAS) is also a powerful technique for obtaining vibrational information about the CO bonding nature of the Pt single-atom catalyst.

REFERENCES

(1) Baroutaji, A.; Carton, J. G.; Sajjia, M.; Olabi, A. G. Materials in PEM Fuel Cells. *Reference Module in Materials Science and Materials Engineering* **2016**. DOI: 10.1016/B978-0-12-803581-8.04006-6.

(2) Gervasio, D. FUEL CELLS - DIRECT ALCOHOL FUEL CELLS | New Materials. *Encyclopedia of Electrochemical Power Sources* **2009**, 420-427. DOI: 10.1016/B978-044452745-5.00247-1.

(3) Oxygen reduction reaction on Pt-based electrocatalysts: Four-electron vs. two-electron pathway. *Chinese Journal of Catalysis* **2022/06/01**, *43* (6). DOI: 10.1016/S1872-2067(21)63961-X.

(4) Tao, J.; Wang, X.; Xu, M.; Liu, C.; Ge, J.; Xing, W. Non-noble metals as activity sites for ORR catalysts in proton exchange membrane fuel cells (PEMFCs). *Industrial Chemistry & Materials* **2023**, *1* (3), 388-409. DOI: 10.1039/d3im00002h (acccessed 2024-03-11T15:11:21).

(5) Matter, P. H.; Ozkan, U. S. Non-metal Catalysts for Dioxygen Reduction in an Acidic Electrolyte. *Catalysis Letters* **2006**, *109* (3-4), 115-123. DOI: 10.1007/s10562-006-0067-1 (acccessed 2024-03-12T17:42:13).

(6) Ertl, G.; Freund, H. J. Catalysis and Surface Science. *Physics Today* **1999**, *52* (1), 32-38. DOI: 10.1063/1.882569 (acccessed 3/13/2024).

(7) Sinar Mashuri, S. I.; Ibrahim, M. L.; Kasim, M. F.; Mastuli, M. S.; Rashid, U.; Abdullah, A. H.; Islam, A.; Asikin Mijan, N.; Tan, Y. H.; Mansir, N.; et al. Photocatalysis for Organic Wastewater Treatment: From the Basis to Current Challenges for Society. *Catalysts* **2020**, *10* (11), 1260. DOI: 10.3390/catal10111260 (acccessed 2024-03-12T20:57:02).

(8) Kolya, H.; Mondal, S.; Kang, C.-W.; Nah, C. The use of polymer-graphene composites in catalysis. *Polymer Nanocomposites Containing Graphene* **2022**, 537-556. DOI: 10.1016/B978-0-12-821639-2.00013-6.

(9) Kamer, P. C. J.; Vogt, D.; Thybaut, J.; Irvine, J. T. S. Introduction to Electrocatalysis. *Contemporary Catalysis: Science, Technology, and Applications* **2017**, 305-325. DOI: 10.1039/9781849739900-00305.

(10) Seeber, R.; Zanardi, C.; Inzelt, G. Links between electrochemical thermodynamics and kinetics. *ChemTexts* **2015**, *1* (4). DOI: 10.1007/s40828-015-0018-9 (acccessed 2024-03-13T14:44:32).

(11) Abedi, E.; Amiri, M. J.; Sahari, M. A. Kinetic, isotherm and thermodynamic investigations on adsorption of trace elements and pigments from soybean oil using high voltage electric field-assisted bleaching: A comparative study. *Process Biochemistry* **2020**, *91*, 208-222. DOI: https://doi.org/10.1016/j.procbio.2019.12.013.

(12) Hashemi, A.; Peljo, P.; Laasonen, K. Understanding Electron Transfer Reactions Using Constrained Density Functional Theory: Complications Due to Surface Interactions. *The Journal of Physical Chemistry C* **2023**, *127* (7), 3398-3407. DOI: 10.1021/acs.jpcc.2c06537.

(13) Si, F.; Zhang, Y.; Yan, L.; Zhu, J.; Xiao, M.; Liu, C.; Xing, W.; Zhang, J. Electrochemical Oxygen Reduction Reaction. Elsevier, 2014; pp 133-170.

(14) Rosen, M. A.; Farsi, A. Electrochemical modeling of batteries. *Battery Technology* **2023**, 65-90. DOI: 10.1016/B978-0-443-18862-6.00007-0.

(15) Aryal, N.; Mørck Ottosen, L. D.; Bentien, A.; Pant, D.; Wegener Kofoed, M. V. Bioelectrochemical systems for biogas upgrading and biomethane production. *Emerging Technologies and Biological Systems for Biogas Upgrading* **2021**, 363-382. DOI: 10.1016/B978-0-12-822808-1.00013-1.

(16) Katz, E. Electrochemical contributions: Julius Tafel (1862–1918). *Electrochemical Science Advances* **2022**, *2* (4). DOI: 10.1002/elsa.202260002 (acccessed 2024-03-13T20:47:22).

(17) Sebastián-Pascual, P.; Jordão Pereira, I.; Escudero-Escribano, M. Tailored electrocatalysts by controlled electrochemical deposition and surface nanostructuring. *Chemical Communications* **2020**, *56* (87), 13261-13272, 10.1039/D0CC06099B. DOI: 10.1039/D0CC06099B.

(18) Perez, N. Mass Transport by Diffusion and Migration. In *Electrochemistry and Corrosion Science*, Springer International Publishing, 2016; pp 151-197.

(19) Wang, N.; Ma, S.; Zuo, P.; Duan, J.; Hou, B. Recent Progress of Electrochemical Production of Hydrogen Peroxide by Two-Electron Oxygen Reduction Reaction. *Advanced Science* **2021**, *8* (15), 2100076. DOI: 10.1002/advs.202100076 (acccessed 2024-03-11T15:06:40).

(20) Hayyan, M.; Hashim, M. A.; Alnashef, I. M. Superoxide Ion: Generation and Chemical Implications. *Chemical Reviews* **2016**, *116* (5), 3029-3085. DOI: 10.1021/acs.chemrev.5b00407 (acccessed 2024-03-11T15:10:01).

(21) Zhang, L.; Jiang, S.; Ma, W.; Zhou, Z. Oxygen reduction reaction on Pt-based electrocatalysts: Four-electron vs. two-electron pathway. *Chinese Journal of Catalysis* **2022**, *43* (6), 1433-1443. DOI: 10.1016/S1872-2067(21)63961-X.

(22) Ma, Z.; Cano, Z. P.; Yu, A.; Chen, Z.; Jiang, G.; Fu, X.; Yang, L.; Wu, T.; Bai, Z.; Lu, J. Enhancing Oxygen Reduction Activity of Pt-based Electrocatalysts: From Theoretical Mechanisms to Practical Methods. *Angewandte Chemie International Edition* **2020**, *59* (42), 18334-18348. DOI: https://doi.org/10.1002/anie.202003654 (acccessed 2024/03/11).

(23) Zhang, W.; Wu, L.; Li, Z.; Liu, Y. Doped graphene: synthesis, properties and bioanalysis. *RSC Advances* **2015**, *5* (61), 49521-49533. DOI: 10.1039/c5ra05051k.

(24) Gao, Y.; Wang, Q.; Ji, G.; Li, A.; Niu, J. Doping strategy, properties and application of heteroatom-doped ordered mesoporous carbon. *RSC Advances* **2021**, *11* (10), 5361-5383. DOI: 10.1039/d0ra08993a (acccessed 2024-03-12T17:30:50).

(25) Ejaz, A.; Jeon, S. The individual role of pyrrolic, pyridinic and graphitic nitrogen in the growth kinetics of Pd NPs on N-rGO followed by a comprehensive study on ORR. *International journal of hydrogen energy* **2018**, *43* (11), 5690-5702. DOI: 10.1016/j.ijhydene.2017.12.184.

(26) Yang, L.; Shui, J.; Du, L.; Shao, Y.; Liu, J.; Dai, L.; Hu, Z. Carbon-Based Metal-Free ORR Electrocatalysts for Fuel Cells: Past, Present, and Future. *Advanced Materials* **2019**, *31* (13), 1804799. DOI: 10.1002/adma.201804799 (acccessed 2024-03-11T22:48:22).

(27) Li, R.; Huang, J.; Li, J.; Cao, L.; Luo, Y.; He, Y.; Lu, G.; Yu, A.; Chen, S. Nitrogen-Doped Hard Carbon on Nickel Foam as Free-Standing Anodes for High-Performance Sodium-Ion Batteries. *ChemElectroChem.* **2020**, *7* (3), 604-613. DOI: 10.1002/celc.201901770.

(28) Arrigo, R.; Schuster, M. E.; Xie, Z.; Yi, Y.; Wowsnick, G.; Sun, L. L.; Hermann, K. E.; Friedrich, M.; Kast, P.; Hävecker, M.; et al. Nature of the N–Pd Interaction in Nitrogen-Doped Carbon Nanotube Catalysts. *ACS Catalysis* **2015**, *5* (5), 2740-2753. DOI: 10.1021/acscatal.5b00094 (acccessed 2024-03-12T17:40:34).

(29) Skorupska, M.; Ilnicka, A.; Lukaszewicz, J. P. The effect of nitrogen species on the catalytic properties of N-doped graphene. *Scientific Reports* **2021**, *11* (1). DOI: 10.1038/s41598-021-03403-8 (acccessed 2024-03-12T00:42:17).

(30) Schweiger, H.; Vayner, E.; Anderson, A. B. Why Is There Such a Small Overpotential for O[sub 2] Electroreduction by Copper Laccase? *Electrochemical and solid-state letters.* **2005**, *8* (11), A585. DOI: 10.1149/1.2050547.

(31) Yang, J.; Liu, W.; Xu, M.; Liu, X.; Qi, H.; Zhang, L.; Yang, X.; Niu, S.; Zhou, D.; Liu, Y.; et al. Dynamic Behavior of Single-Atom Catalysts in Electrocatalysis: Identification of Cu-N3 as an Active Site for the Oxygen Reduction Reaction. *Journal of the American Chemical Society* **2021**, *143* (36), 14530-14539. DOI: 10.1021/jacs.1c03788.

(32) Li, W.; Min, C.; Tan, F.; Li, Z.; Zhang, B.; Si, R.; Xu, M.; Liu, W.; Zhou, L.; Wei, Q.; et al. Bottom-Up Construction of Active Sites in a Cu–N4–C Catalyst for Highly Efficient Oxygen Reduction Reaction. *ACS Nano* **2019**, *13* (3), 3177-3187. DOI: 10.1021/acsnano.8b08692.

(33) Maillard, F.; Eikerling, M.; Cherstiouk, O. V.; Schreier, S.; Savinova, E.; Stimming, U. Size effects on reactivity of Pt nanoparticles in CO monolayer oxidation: The role of surface mobility. *Faraday Discussions* **2004**, *125* (0), 357-377, 10.1039/B303911K. DOI: 10.1039/B303911K.

(34) Koper, M. T. M.; Jansen, A. P. J.; Van Santen, R. A.; Lukkien, J. J.; Hilbers, P. A. J. Monte Carlo simulations of a simple model for the electrocatalytic CO oxidation on platinum. *The Journal of Chemical Physics* **1998**, *109* (14), 6051-6062. DOI: 10.1063/1.477230 (acccessed 2024-03-14T19:32:01).

(35) Vielstich, W.; Lamm, A.; Gasteiger, H. A.; Yokokawa, H.; Iwasita, T.; Ciapina, E. G. Abstract. *Handbook of Fuel Cells* **2010**. DOI: 10.1002/9780470974001.f500014.

(36) Ciapina, E. G.; Santos, S. F.; Gonzalez, E. R. Electrochemical CO stripping on nanosized Pt surfaces in acid media: A review on the issue of peak multiplicity. *Journal of Electroanalytical Chemistry* **2018**, *815*, 47-60. DOI: 10.1016/j.jelechem.2018.02.047.

(37) He, Y.; Wu, G. PGM-Free Oxygen-Reduction Catalyst Development for Proton-Exchange Membrane Fuel Cells: Challenges, Solutions, and Promises. *Accounts of Materials Research* **2022**, *3* (2), 224-236. DOI: 10.1021/accountsmr.1c00226.

(38) Chen, Y.; Huang, Z.; Ma, Z.; Chen, J.; Tang, X. Fabrication, characterization, and stability of supported single-atom catalysts. *Catalysis Science & Technology* **2017**, *7* (19), 4250-4258. DOI: 10.1039/c7cy00723j.

(39) Zheng, X.; Yang, J.; Wang, D. Advanced dual-atom catalysts for efficient oxygen evolution reaction. *EES Catalysis* **2023**, *1* (5), 665-676. DOI: 10.1039/d3ey00050h.

(40) Zhang, J.; Chen, G.; Müllen, K.; Feng, X. Carbon-Rich Nanomaterials: Fascinating Hydrogen and Oxygen Electrocatalysts. *Advanced Materials* **2018**, *30* (40), 1800528. DOI: 10.1002/adma.201800528.

(41) Yin, P.; Yao, T.; Wu, Y.; Zheng, L.; Lin, Y.; Liu, W.; Ju, H.; Zhu, J.; Hong, X.; Deng, Z.; et al. Single Cobalt Atoms with Precise N-Coordination as Superior Oxygen Reduction Reaction Catalysts. *Angewandte Chemie International Edition* **2016**, *55* (36), 10800-10805. DOI: 10.1002/anie.201604802.

(42) Yao, C.; Guo, N.; Xi, S.; Xu, C.-Q.; Liu, W.; Zhao, X.; Li, J.; Fang, H.; Su, J.; Chen, Z.; et al. Atomically-precise dopant-controlled single cluster catalysis for electrochemical nitrogen reduction. *Nature Communications* **2020**, *11* (1). DOI: 10.1038/s41467-020-18080-w.

(43) Wang, S.; Yu, D.; Dai, L.; Chang, D. W.; Baek, J.-B. Polyelectrolyte-Functionalized Graphene as Metal-Free Electrocatalysts for Oxygen Reduction. *ACS Nano* **2011**, *5* (8), 6202-6209. DOI: 10.1021/nn200879h.

(44) Fikry, M.; Tawfik, W.; Omar, M. M. Investigation on the effects of laser parameters on the plasma profile of copper using picosecond laser induced plasma spectroscopy. *Optical and Quantum Electronics* **2020**, *52* (5). DOI: 10.1007/s11082-020-02381-x.

(45) Sahai, A.; Goswami, N.; Kaushik, S. D.; Tripathi, S. Cu/Cu2O/CuO nanoparticles: Novel synthesis by exploding wire technique and extensive characterization. *Applied Surface Science* **2016**, *390*, 974-983. DOI: 10.1016/j.apsusc.2016.09.005.

(46) Cai, Y.; Fu, J.; Zhou, Y.; Chang, Y.-C.; Min, Q.; Zhu, J.-J.; Lin, Y.; Zhu, W. Insights on forming N,O-coordinated Cu single-atom catalysts for electrochemical reduction CO2 to methane. *Nature Communications* **2021**, *12* (1). DOI: 10.1038/s41467-020-20769-x.

(47) Bulushev, D. A.; Chuvilin, A. L.; Sobolev, V. I.; Stolyarova, S. G.; Shubin, Y. V.; Asanov, I. P.; Ishchenko, A. V.; Magnani, G.; Riccò, M.; Okotrub, A. V.; Bulusheva, L. G. Copper on carbon materials: stabilization by nitrogen doping. *Journal of Materials Chemistry A* **2017**, *5* (21), 10574-10583. DOI: 10.1039/c7ta02282d.

(48) Lai, L.; Potts, J. R.; Zhan, D.; Wang, L.; Poh, C. K.; Tang, C.; Gong, H.; Shen, Z.; Lin, J.; Ruoff, R. S. Exploration of the active center structure of nitrogen-doped graphene-based catalysts for oxygen reduction reaction. *Energy & Environmental Science* **2012**, *5* (7), 7936. DOI: 10.1039/c2ee21802j.

(49) Matanovic, I.; Artyushkova, K.; Strand, M. B.; Dzara, M. J.; Pylypenko, S.; Atanassov, P. Core Level Shifts of Hydrogenated Pyridinic and Pyrrolic Nitrogen in the Nitrogen-Containing Graphene-Based Electrocatalysts: In-Plane vs Edge Defects. *The Journal of Physical Chemistry C* **2016**, *120* (51), 29225-29232. DOI: 10.1021/acs.jpcc.6b09778.

(50) Artyushkova, K. Misconceptions in interpretation of nitrogen chemistry from x-ray photoelectron spectra. *Journal of Vacuum Science & Technology A: Vacuum, Surfaces, and Films* **2020**, *38* (3), 031002. DOI: 10.1116/1.5135923.

(51) Han, G.; Zheng, Y.; Zhang, X.; Wang, Z.; Gong, Y.; Du, C.; Banis, M. N.; Yiu, Y.-M.; Sham, T.-K.; Gu, L.; et al. High loading single-atom Cu dispersed on graphene for efficient oxygen reduction reaction. *Nano Energy* **2019**, *66*, 104088. DOI: 10.1016/j.nanoen.2019.104088.

(52) Wang, X.; Zhu, R.; Dai, Y.; Xia, H.; Niu, Q. N-Hydroxyethyl-2-Pyrrolidone Improved Cu-Based Catalysts with High Performance for Acetylene Hydrochlorination. *Catalysis Letters* **2023**. DOI: 10.1007/s10562-023-04463-3.

(53) Favaro, M.; Xiao, H.; Cheng, T.; Goddard, W. A.; Yano, J.; Crumlin, E. J. Subsurface oxide plays a critical role in CO$_2$ activation by Cu(111) surfaces to form chemisorbed CO$_2$, the first step in reduction of CO$_2$. *Proceedings of the National Academy of Sciences* **2017**, *114* (26), 6706-6711. DOI: 10.1073/pnas.1701405114.

(54) Cui, L.; Cui, L.; Li, Z.; Zhang, J.; Wang, H.; Lu, S.; Xiang, Y. A copper single-atom catalyst towards efficient and durable oxygen reduction for fuel cells. *Journal of Materials Chemistry A* **2019**, *7* (28), 16690-16695. DOI: 10.1039/c9ta03518d.

(55) Ji, S.; Chen, Y.; Wang, X.; Zhang, Z.; Wang, D.; Li, Y. Chemical Synthesis of Single Atomic Site Catalysts. *Chemical Reviews* **2020**, *120* (21), 11900-11955. DOI: 10.1021/acs.chemrev.9b00818.

(56) <3-acid leaching.pdf>.

(57) Yang, Z.-H.; Cao, J.-P.; Zhuang, Q.-Q.; Wu, Y.; Zhou, Z.; Wei, Y.-L.; Zhao, X.-Y. Oxygen-enriched porous carbon derived from acid washed and oxidized lignite via H3PO4 hydrothermal for high-performance supercapacitors. *Fuel Processing Technology* **2023**, *243*, 107665. DOI: 10.1016/j.fuproc.2023.107665.

(58) Cheng, Q.; Chen, W.; Dai, H.; Liu, Y.; Dong, X. Energy storage performance of electric double layer capacitors with gradient porosity electrodes. *Journal of Electroanalytical Chemistry* **2021**, *889*, 115221. DOI: 10.1016/j.jelechem.2021.115221.

(59) Lin, C.; Compton, R. G. Understanding mass transport influenced electrocatalysis at the nanoscale via numerical simulation. *Current Opinion in Electrochemistry* **2019**, *14*, 186-199. DOI: 10.1016/j.coelec.2018.08.001.

(60) Biemolt, J.; Rothenberg, G.; Yan, N. Understanding the roles of amorphous domains and oxygen-containing groups of nitrogen-doped carbon in oxygen reduction catalysis: toward superior activity. *Inorganic Chemistry Frontiers* **2020**, *7* (1), 177-185. DOI: 10.1039/c9qi00983c.

(61) Wang, J.; Zhao, C.-X.; Liu, J.-N.; Ren, D.; Li, B.-Q.; Huang, J.-Q.; Zhang, Q. Quantitative kinetic analysis on oxygen reduction reaction: A perspective. *Nano Materials Science* **2021**, *3* (3), 313-318. DOI: 10.1016/j.nanoms.2021.03.006.

(62) Nagappan, S.; Duraivel, M.; Han, S.; Yusuf, M.; Mahadadalkar, M.; Park, K.; Dhakshinamoorthy, A.; Prabakar, K.; Park, S.; Ha, C.-S.; et al. Electrocatalytic Oxygen Reduction Reaction of Graphene Oxide and Metal-Free Graphene in an Alkaline Medium. *Nanomaterials* **2023**, *13* (8), 1315. DOI: 10.3390/nano13081315.

(63) Platzman, I.; Brener, R.; Haick, H.; Tannenbaum, R. Oxidation of Polycrystalline Copper Thin Films at Ambient Conditions. *The Journal of Physical Chemistry C* **2008**, *112* (4), 1101-1108. DOI: 10.1021/jp076981k.

(64) Pardo Pérez, L. C.; Arndt, A.; Stojkovikj, S.; Ahmet, I. Y.; Arens, J. T.; Dattila, F.; Wendt, R.; Guilherme Buzanich, A.; Radtke, M.; Davies, V.; et al. Determining Structure-Activity Relationships in Oxide Derived Cu☐Sn Catalysts During CO2 Electroreduction Using X-Ray Spectroscopy. *Advanced Energy Materials* **2021**, *12* (5). DOI: 10.1002/aenm.202103328.

(65) He, L.; Li, J.; Wu, X.; Mu, F.; Wang, Y.; Lu, Y.; Suga, T. Robust Ag-Cu Sintering Bonding at 160 °C via Combining Ag2O Microparticle Paste and Pt-Catalyzed Formic Acid Vapor. *Metals* **2020**, *10* (3). DOI: 10.3390/met10030315.

(66) Xia, C.; Qiu, Y.; Xia, Y.; Zhu, P.; King, G.; Zhang, X.; Wu, Z.; Kim, J. Y. T.; Cullen, D. A.; Zheng, D.; et al. General synthesis of single-atom catalysts with high metal loading using graphene quantum dots. *Nat Chem* **2021**, *13* (9), 887-894. DOI: 10.1038/s41557-021-00734-x From NLM PubMed-not-MEDLINE.

(67) Kossmann, J.; Ortíz Sánchez-Manjavacas, M. L.; Zschiesche, H.; Tarakina, N. V.; Antonietti, M.; Albero, J.; López-Salas, N. Cu^{II}/Cu^{I} decorated

N-doped carbonaceous electrocatalysts for the oxygen reduction reaction. *Journal of Materials Chemistry A* **2022**, *10* (11), 6107-6114. DOI: 10.1039/d1ta09459a.

(68) Novikova, K.; Kuriganova, A.; Leontyev, I.; Gerasimova, E.; Maslova, O.; Rakhmatullin, A.; Smirnova, N.; Dobrovolsky, Y. Influence of Carbon Support on Catalytic Layer Performance of Proton Exchange Membrane Fuel Cells. *Electrocatalysis* **2018**, *9* (1), 22-30. DOI: 10.1007/s12678-017-0416-4.

(69) Lončar, A.; Jovanovič, P.; Hodnik, N.; Gaberšček, M. Determination of the Electroactive Surface Area of Supported Ir-Based Oxygen Evolution Catalysts by Impedance Spectroscopy: Observed Anomalies with Respect to Catalyst Loading. *Journal of The Electrochemical Society* **2023**, *170* (4), 044504. DOI: 10.1149/1945-7111/accaad (acccessed 2024-03-15T18:24:35).

(70) Dupont, M.; Hollenkamp, A. F.; Donne, S. W. Electrochemically active surface area effects on the performance of manganese dioxide for electrochemical capacitor applications. *Electrochimica Acta* **2013**, *104*, 140-147. DOI: https://doi.org/10.1016/j.electacta.2013.04.007.

(71) Bae, G.; Kim, H.; Choi, H.; Jeong, P.; Kim, D. H.; Kwon, H. C.; Lee, K.-S.; Choi, M.; Oh, H.-S.; Jaouen, F.; Choi, C. H. Quantification of Active Site Density and Turnover Frequency: From Single-Atom Metal to Nanoparticle Electrocatalysts. *JACS Au* **2021**, *1* (5), 586-597. DOI: 10.1021/jacsau.1c00074 (acccessed 2024-03-31T00:43:31).

(72) Gong, M.; Mehmood, A.; Ali, B.; Nam, K.-W.; Kucernak, A. Oxygen Reduction Reaction Activity in Non-Precious Single-Atom (M–N/C) Catalysts─Contribution of Metal and Carbon/Nitrogen Framework-Based Sites. *ACS Catalysis* **2023**, *13* (10), 6661-6674. DOI: 10.1021/acscatal.3c00356 (acccessed 2024-03-31T02:30:01).

(73) Li, J.; Chen, C.; Xu, L.; Zhang, Y.; Wei, W.; Zhao, E.; Wu, Y.; Chen, C. Challenges and Perspectives of Single-Atom-Based Catalysts for Electrochemical Reactions. *JACS Au* **2023**, *3* (3), 736-755. DOI: 10.1021/jacsau.3c00001.

(74) Liu, J.; Wang, J.; Xu, C.; Jiang, H.; Li, C.; Zhang, L.; Lin, J.; Shen, Z. X. Advanced Energy Storage Devices: Basic Principles, Analytical Methods, and Rational Materials Design. *Advanced Science* **2018**, *5* (1), 1700322. DOI: 10.1002/advs.201700322.

(75) Röttcher, N. C.; Ku, Y.-P.; Minichova, M.; Ehelebe, K.; Cherevko, S. Comparison of methods to determine electrocatalysts' surface area in gas diffusion electrode setups: a case study on Pt/C and PtRu/C. *Journal of Physics: Energy* **2023**, *5* (2), 024007. DOI: 10.1088/2515-7655/acbe1b.

(76) Chen, D.; Li, Y.; Xiao, S.; Yang, C.; Zhou, J.; Xiao, B. Single Ni atom doped WS2 monolayer as sensing substrate for dissolved gases in transformer oil: A first-principles study. *Applied Surface Science* **2022**, *579*, 152141. DOI: https://doi.org/10.1016/j.apsusc.2021.152141.

(77) Shi, Y.; Ma, Z.-R.; Xiao, Y.-Y.; Yin, Y.-C.; Huang, W.-M.; Huang, Z.-C.; Zheng, Y.-Z.; Mu, F.-Y.; Huang, R.; Shi, G.-Y.; et al. Electronic metal–support interaction modulates single-atom platinum catalysis for hydrogen evolution reaction. *Nature Communications* **2021**, *12* (1). DOI: 10.1038/s41467-021-23306-6.

(78) Gasteiger, H. A.; Markovic, N.; Ross, P. N., Jr.; Cairns, E. J. Carbon monoxide electrooxidation on well-characterized platinum-ruthenium alloys. *The Journal of Physical Chemistry* **1994**, *98* (2), 617-625. DOI: 10.1021/j100053a042.

(79) Yang, L.; Zhu, X.; Xiong, S.; Wu, X.; Shan, Y.; Chu, P. K. Synergistic WO3·2H2O Nanoplates/WS2 Hybrid Catalysts for High-Efficiency Hydrogen Evolution. *ACS Applied Materials & Interfaces* **2016**, *8* (22), 13966-13972. DOI: 10.1021/acsami.6b04045.

Dawatage Shashika Madushani Perera

Education

BSc, Chemistry, Biochemistry, Botany   2017
University of Kelaniya.   Sri Lanka

Master of Science in Industrial Analytical Chemistry   2020
University of Sri Jayewardenepura, Nugegoda.   Sri Lanka

Publications

Dawatage Shashika Madushani Perera, Prakhar Sharma, Nadeesha Kothalawala, Ayanthi Thisera, Doo Young Kim, Copper-incorporated graphene-quantum dot derived single-atom catalyst for oxygen reduction reaction. – In preparation.

D. S. M. Perera, R. C. L. De Silva, L. D. C. Nayanajith, H. C. D. P. Colombage, T. S. Suresh, W. P. K. M. Abeysekera and I. R. M. Kottegoda, "Anti-Inflammatory and Antioxidant Properties of Coffea Arabica/Reduced Graphene Oxide Nanocomposite Prepared by Green Synthesis," Mat. Sci. Res. India, 18, pp. 305-317, (2021). http://dx.doi.org/10.13005/msri/180306

Patent

I.R.M. Kottegoda, **D.S.M. Perera**, H.C.D.P. Colombage, R.C.L. De Silva and L.D.C. Nayanajith, Coffea-arabica /graphene nanocomposite with effective antioxidant and anti-inflammatory properties for biomedical application and preparation method thereof, Sri Lanka Patent No. 22011 (2021).